The Astrophysical Journal, 897:176 (19pp), 2020 July 10 https://doi.org/10.3847/1538-4357/ab9c23

The Molecular Interstellar Medium in the Super Star Clusters of the Starburst NGC 253

Nico Krieger[1], Alberto D. Bolatto[2], Adam K. Leroy[3], Rebecca C. Levy[2], Elisabeth A. C. Mills[4], David S. Meier[5,6], Jürgen Ott[6], Sylvain Veilleux[2], Fabian Walter[1,6], and Axel Weiß[7]
[1] Max-Planck-Institut für Astronomie, Königstuhl 17, D-69120 Heidelberg, Germany; krieger@mpia.de
[2] Department of Astronomy, University of Maryland, College Park, MD 20742, USA
[3] Department of Astronomy, The Ohio State University, 4055 McPherson Laboratory, 140 West 18th Avenue, Columbus, OH 43210, USA
[4] Physics Department, Brandeis University, 415 South Street, Waltham, MA 02453, USA
[5] New Mexico Institute of Mining and Technology, 801 Leroy Place, Socorro, NM 87801, USA
[6] National Radio Astronomy Observatory, P.O. Box O, 1003 Lopezville Road, Socorro, NM 87801, USA
[7] Max-Planck-Institut für Radioastronomie, Auf dem Hügel 69, D-53121 Bonn, Germany
Received 2019 October 15; revised 2020 June 9; accepted 2020 June 10; published 2020 July 16

Abstract

We present submillimeter spectra of the (proto-)super star cluster (SSC) candidates in the starbursting center of the nearby galaxy NGC 253 identified by Leroy et al. The 2.5 pc resolution of our Atacama Large Millimeter/submillimeter Array cycle 3 observations approaches the size of the SSCs and allows for the study of physical and chemical properties of the molecular gas in these sources. In the 14 SSC sources and in the frequency ranges 342.0–345.8 GHz and 353.9–357.7 GHz, we detect 55 lines belonging to 19 different chemical species. The SSCs differ significantly in chemical complexity, with the richest clusters showing 19 species and the least complex showing four species. We detect HCN isotopologues and isomers ($H^{13}CN$, $HC^{15}N$, $H^{15}NC$), abundant HC_3N, SO and $S^{18}O$, SO_2, and H_2CS. The gas ratios CO/HCN, CO/HCO^+ are low, ∼1–10, implying high dense gas fractions in the SSCs. Line ratio analyses suggests chemistry consistent with photon-dominated regions and mechanical heating. None of the SSCs near the galaxy center show line ratios that imply an X-ray-dominated region, suggesting that heating by any (still unknown) active galactic nucleus does not play a major role. The gas temperatures are high in most sources, with an average rotational temperature of ∼130 K in SO_2. The widespread existence of vibrationally excited HCN and HC_3N transitions implies strong infrared radiation fields, potentially trapped by a greenhouse effect due to high continuum opacities.

Unified Astronomy Thesaurus concepts: Starburst galaxies (1570); Astrochemistry (75); Star clusters (1567); Dense interstellar clouds (371); Interstellar medium (847); Star formation (1569)

Supporting material: data behind figure, figure set, machine-readable tables

1. Introduction

Super star clusters (SSCs) are massive ($M_* > 10^5\ M_\odot$), compact (R ∼ 1 pc) clusters of stars. They are frequently found in starbursts in the centers of galaxies or galaxy mergers, such as M 82, NCG 253 or the Antennae galaxies (e.g., Holtzman et al. 1992; Whitmore 2003; McCrady et al. 2005; Portegies Zwart et al. 2010; Leroy et al. 2018). The stellar properties of SSCs are similar to Galactic globular clusters, and thus SSCs might represent a younger generation of the same sort of stellar systems (e.g., Gorjian et al. 2001; Portegies Zwart et al. 2010). The extreme conditions under which SSCs form are rare in the present-day universe but are thought to be common around the peak of the cosmic star formation rate (SFR) history, the era when most of today's globular clusters formed. Hence, observations of forming SSCs might offer a glimpse into the physics of a mode of star formation (SF) common in the early universe.

NGC 253 is one of the nearest starburst systems, at a distance of 3.5 Mpc (Rekola et al. 2005). It is considered one of the prototypical starburst galaxies, with an SFR of $\sim 2\ M_\odot\ yr^{-1}$ in its center (Ott et al. 2005; Leroy et al. 2015; Bendo et al. 2015). NGC 253 has a prominent bar that feeds gas to the nuclear starburst (Sorai et al. 2000; Paglione et al. 2004). The gas flows lead to intense SF, which creates feedback driving outflows that have been detected across the spectrum from X-ray to radio wavelengths in ionized, neutral, and molecular gas (Turner 1985; Heckman et al. 2000; Strickland et al. 2000, 2002; Sharp & Bland-Hawthorn 2010; Sturm et al. 2011; Westmoquette et al. 2011; Bolatto et al. 2013; Walter et al. 2017; Krieger et al. 2019).

It has been known for a while now that NGC 253 hosts an SSC. Watson et al. (1996) and Kornei & McCrady (2009) detected a young, deeply embedded SSC in Hubble Space Telescope imaging of the nuclear region. Hints of further SSCs were discovered in radio observations (Ulvestad & Antonucci 1997) but do not show obvious counterparts in optical or near-IR imaging (Walter et al. 2017). The massive and dense molecular clouds in NGC 253 seen in the millimeter and submillimeter (e.g., Sakamoto et al. 2011; Leroy et al. 2015; Meier et al. 2015) provide an ideal environment for SSC formation. Ando et al. (2017) showed that massive SF is indeed present in small (<10 pc) gas clumps identified from Atacama Large Millimeter/submillimeter Array (ALMA) observations. Utilizing even higher-resolution ALMA observations, Leroy et al. (2018, hereafter L18) characterized 14 proto-SSCs still deeply embedded in their natal gas and dust clouds. At least some of these SSCs are very young (<1 Myr; Rico-Villas et al. 2020), with many showing roughly equal, but still uncertain, masses of young stars and gas (L18).

Due to its proximity, NGC 253 is an ideal target for high-resolution studies of the physics and chemistry of the star-forming gas in starbursts. Several studies of the chemical environment in NGC 253 have been carried out but none of them had the resolution to approach the scale of stellar clusters (e.g., Martin et al. 2006; Aladro et al. 2015; Meier et al. 2015; Mangum et al. 2019). In this article, we utilize high-resolution

(2.5 pc, 0.″15) ALMA observations in band 7 (∼350 GHz) to study the physical and chemical environment of individual embedded (proto-)SSC candidates.

In deep imaging, we detect up to 19 molecular species with up to 55 spectral lines over 7.6 GHz bandwidth (342.0–345.8 GHz, 353.9–357.7 GHz) in each SSC. Among the detected species are commonly used dense gas tracers, potential photo-dominated region (PDR) tracers, optically thin isotopologues, and vibrationally excited species. These spectral lines and the ratios among them are sensitive to the physical and chemical interstellar medium (ISM) properties. They depend on heating and cooling of the gas, the energy source, ionization, or radiation properties such as the infrared (IR) field through nonthermal excitation or radiative pumping. Together, the inferred properties determine the state of the natal gas clouds of the SSCs and the early feedback exerted on them.

This article is structured as follows: Section 2 describes the observations, data reduction, and line identification. The procedure of fitting the spectra is laid out in Section 3, which also shows the fitted spectra. The results are interpreted and discussed in Section 4. We conclude with a summary in Section 5. Appendices A–B list the details of spectral fitting, present the fitted spectra of all sources, and list obtained quantities.

2. Data Reduction

2.1. Observations, Calibration, and Imaging

Data reduction and imaging of our ALMA cycle 4 observations are described in detail in Krieger et al. (2019). Though that study presented only the narrow frequency range containing the CO(3–2) line, we applied the same data reduction described there to the whole observed lower and upper sidebands (LSBs, USBs). The sidebands are tuned to 342.0–345.8 GHz (LSB) and 353.9–357.7 GHz (USB), yielding a combined 7.6 GHz total bandwidth.

The pipeline-calibrated and continuum-subtracted visibilities are imaged in 2.5 MHz channels (∼2.5 km s^{-1} at ∼350 GHz) using Briggs weighting (robust parameter of 0.5). The synthesized beam varies only slightly between LSBs and USBs (∼2% linear deviation, ∼4% beam area deviation), so both bands are restored with the same beam of 0.″17 × 0.″13. This offers the benefit of identical resolution in both bands. The per-channel noise is 0.37 K.

Line crowding left us with limited bandwidth to fit the continuum, and as a result the initial continuum subtraction in the *u*, *v* plane left a low level of residual continuum in the USB for some sources (SSCs 2, 5, 8, 10, 13, 14). To account for this, we also carry out an image-plane continuum subtraction for the affected spectra. As the line-free ranges are small in some sources in the USB, the errors in the continuum fits can be substantial, up to ∼0.2 K. This can be relevant for our faintest detected lines, which have brightness $\lesssim$2 K. In this case, the uncertainty due to the continuum is of the same order as the uncertainty as the flux calibration. For brighter lines and the LSB, the uncertainty in the continuum subtraction is negligible.

2.2. Spectra

We aim to constrain the physical and chemical properties of the SSCs identified by L18. They found the sizes of the SSCs to be of the order of the beam size (deconvolved sizes of ∼1.5–4 pc). Therefore, we extract single-pixel (0.″1 × 0.″1) spectra at the recorded center positions.

For easier handling of spectra, we shift the spectral axis from the observed frequency to the rest-frame frequency. The CS(7–6) line provides a good estimate for the systemic velocity of the SSCs. It is clearly detected in all sources and does not show complex line profiles. In some sources, CS(7–6) has multiple velocity components but one component clearly dominates. We use this dominant component as the reference. We estimate the velocity from a Gaussian fit and apply the Doppler correction to shift to the rest frequency. Our estimates of the source velocities are consistent within $<$5 km s^{-1} with L18, who used an independently imaged version of the same observations.

In SSC 3, two peaks of close to equal peak intensity do not allow for a robust determination of the source velocity. There we obtain a combined estimate from the H^{15}NC, SO, and H^{13}CN lines. Including these lines neither improves, nor worsens the velocity estimate for the other sources.

Note that the spectral fits described in Section 3 still have the velocity centroid as a free parameter. This allows us to detect shifts of lines relative to each other.

Figure 1 shows an overview of the spectra. Zoom-ins are given in Figure 2 and Figure Set 2.

2.3. Line Identification

We identified the spectral lines in our spectra with the help of Splatalogue[8] (Remijan et al. 2007) using data from the Cologne Database for Molecular Spectroscopy (CDMS;[9] Müller et al. 2005) and Jet Propulsion Laboratory (JPL; Pickett et al. 1998) catalogs. Spectra centered on the bright continuum sources were examined independently by four investigators and guided by lower-resolution observations in the literature. The lines consistently identified by all investigators form the final line list (Table 1) that we use in this article. We mark vibrationally excited spectral lines by an asterisk or give the exact vibrational state.

Note that our line identification is conservative. Some spectra show faint features not included as identified lines (see Figure 2). We do not analyze these further in this paper.

3. Spectral Line Fitting with XCLASS

As lines of the same or different species are blended in the spectra, an integration over a line over a fixed velocity range will overestimate the actual intensity of the line. We therefore optimize model spectra to the observed spectra using the eXtended CASA Line Analysis Software Suite (XCLASS;[10] Möller et al. 2018). This method requires some physical assumptions about the emission but yields a physical interpretation of the spectra, for instance column density or excitation temperature. It further allows us to de-blend the spectra and unambiguously derive observational properties such as integrated intensity. Table 1 lists the 55 lines that we fit for.

3.1. Treatment of Multiple Spectral Components

The CO(3–2), HCN(4–3), HCO$^+$(4–3), and CS(7–6) lines show multiple peaks of varying strength in the spectra whereas all

[8] https://www.cv.nrao.edu/php/splat
[9] https://cdms.astro.uni-koeln.de/
[10] https://xclass.astro.uni-koeln.de/Home

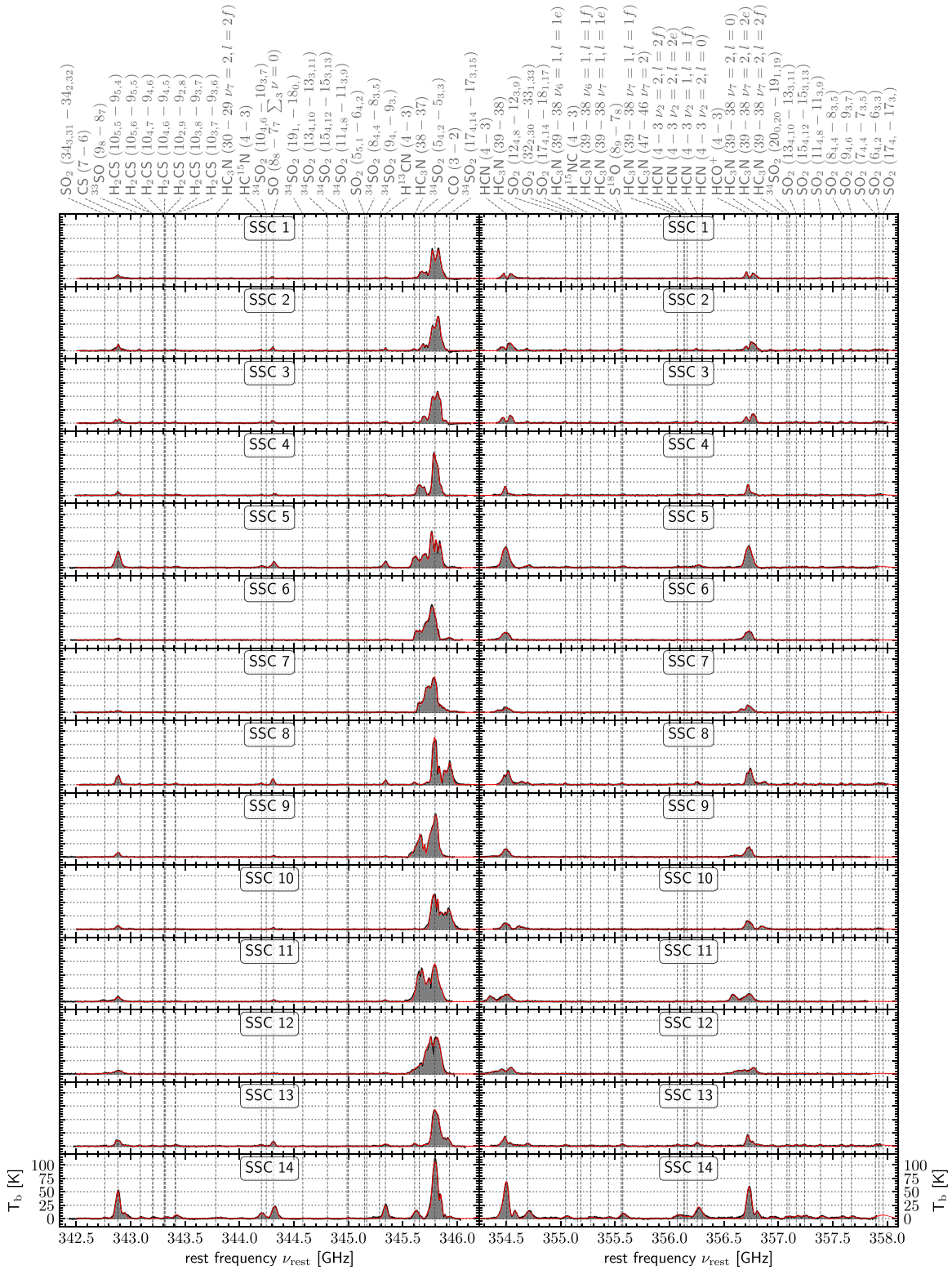

Figure 1. Overview and relative comparison of the spectra (black) and XCLASS fits (red) of the 14 SSCs. Note that the frequency axis is presented as rest frequency to allow for easier interpretation of the spectra (see Section 2.2). The detected species are labeled at the top. A zoom-in of this figure is given in Figure Set 2 and Figure 2 for SSC 14.

(The data used to create this figure are available.)

other lines do not show noticeable deviations from Gaussian shapes within noise limits. From the line profiles alone, it is impossible to decide if a double peak seen in a line is the result of multiple emission components or absorption. For consistency, we assume that the spectra are composed of emission components only and try to model them with as few components as necessary.

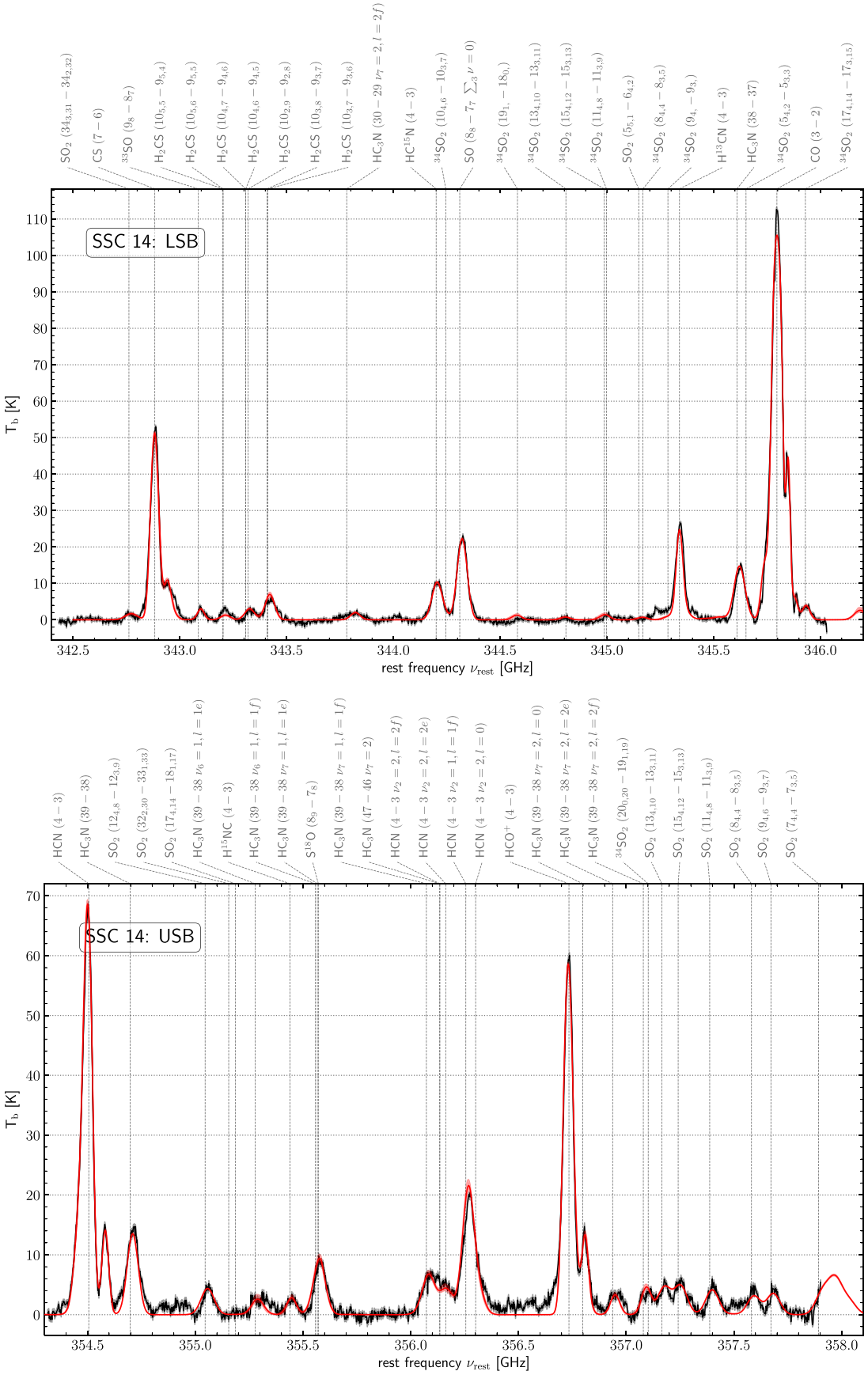

Figure 2. Spectra of SSC 14 in the LSB (*top*) and USB (*bottom*). This figure set shows a zoom of the bottom two panels of Figure 1. The observed spectrum (black) sits on top of a gray band indicating the 16th–84th percentiles of the noise added for error estimation in the fit (see Section 3.3). The red lines represent the median fit obtained by XCLASS using the fitting procedure described in Section 3.2. The Monte Carlo–estimated errors are shown as a red band (16th–84th percentiles) that is hardly visible due to its small size relative to the strong spectral lines.

(The complete figure set (14 images) is available.)

Table 1
Sample of the Fitted Integrated Intensities in Kelvin kilometers per second

Molecule	Transition		Comp.[a]	SSC No.													
	Rotational	Vibrational		1	2	3	4	5	6	7	8	9	10	11	12	13	14
CO	3–2	$\nu = 0$	0	810	684	167	744	1607	199	149	1361	188	3004	1451	4132	161	127
CO	3–2	$\nu = 0$	1	1741	2328	1692	788	1014	3509	249	394	2919	418	2978	2962	3552	197
CO	3–2	$\nu = 0$	2	1737	1698	568	2654	2048	1862	324	702	2308	1462	1148	1749	1114	806
CO	3–2	$\nu = 0$	3	288	245	2187	724	1452	302	2678	496	212	2103	959	575	904	5486
CO	3–2	$\nu = 0$	4	551	367	544	501	1030	491	3327	3578	1096	747	1148	762	406	517
CO	3–2	$\nu = 0$	5	…	…	…	…	…	…	572	232	1282	…	2593	…	…	…
HCO^+	4–3	$\nu = 0$	0	366	736	630	321	2460	638	527	812	327	884	463	616	604	246
HCO^+	4–3	$\nu = 0$	1	278	212	333	352	…	499	157	647	840	295	600	391	153	2591
HCO^+	4–3	$\nu = 0$	2	…	…	…	43	…	…	209	280	208	…	715	317	104	…
HCN	4–3	$\nu = 0$	0	354	727	547	234	2230	1021	263	798	406	736	556	678	267	477
HCN	4–3	$\nu = 0$	1	201	127	286	324	…	…	209	569	537	290	581	404	398	2399
HCN	4–3	$\nu = 0$	2	…	…	…	…	…	…	178	289	137	…	527	280	124	…
HCN	4–3	$\nu_2 = 2, l = 2f$	0	6	25	12	28	28	…	…	9	…	…	…	…	41	141
HCN	4–3	$\nu_2 = 2, l = 2e$	0	6	25	12	28	28	…	…	9	…	…	…	…	41	136
HCN	4–3	$\nu_2 = 2, l = 0$	0	9	36	17	40	39	…	…	13	…	…	…	…	59	197
HCN	4–3	$\nu_2 = 1, l = 1f$	0	55	127	93	79	283	…	…	212	…	…	34	…	288	1179
$H^{13}CN$	4–3	$\nu = 0$	0	32	53	41	13	370	34	…	177	51	11	92	69	124	697
$HC^{15}N$	4–3	$\nu = 0$	0	…	61	52	22	167	…	…	76	…	…	…	…	130	534
$H^{15}NC$	4–3	$\nu = 0$	0	17	39	31	…	71	…	…	27	…	…	…	…	37	135
CS	7–6	$\nu = 0$	0	97	103	61	209	1452	118	126	654	337	238	498	551	282	2116
CS	7–6	$\nu = 0$	1	172	268	132	…	…	…	40	…	…	79	…	…	238	285
CS	7–6	$\nu = 0$	2	…	…	151	…	…	…	…	…	…	…	…	…	54	…

Notes. The typical intensity error is 13.0% and consists primarily of uncertainty due to line crowding. Additionally, the systematic flux uncertainty applies with $\lesssim$5% for these observations according to the ALMA specifications.

[a] Components do not necessarily correspond to each other. For instance, the undetected marks (…) for component 5 of CO(3–2) in SSC 1 merely indicate that five components fit the spectrum sufficiently well whereas in SSC 7 six components are required.

(This table is available in its entirety in machine-readable form.)

In CO(3–2), five or six components are required while in HCN (4–3), HCO^+(4–3), and CS(7–6), up to three components suffice to achieve a good fit. Upon closer inspection of the fit results below, it seems likely that the appearance of multiple components in a few cases is at least partially caused by absorption. In the following, "main component" denotes the velocity component closest to the source's systemic velocity (as defined by the brightest CS(7–6) peak and consistent with the single component species, see Section 2.2), which is usually also the brightest component.

3.2. Spectral Fitting Procedure

The observed spectral lines originate from (rotationally or vibrationally) excited molecular gas with excitation temperature T_{ex} and column density N. The dependence of observed line amplitude, width, and shape on T_{ex} and N is complex and requires solving the radiative transfer. This task is simplified substantially by software tools and the availability of cataloged line properties. In this work, we use XCLASS for this task. XCLASS models input data by solving the radiative transfer equation for an isothermal object in one dimension and optimizes the model using the MAGIX optimizer to fit the data. The molecular parameters required for this task are obtained from the CDMS catalog.

The complexity of fitting up to 55 lines with $n \times 55$ parameters is challenging and cannot reliably be done in one go. We instead employ a three-step method to obtain the best possible results: (1) an unconstrained, independent XCLASS fit of each species individually for each source, followed by (2) a joint fit of all detected species to the whole data range for each source, and (3) refinement fits for selected species while keeping all other species fixed.

In the first run, we fit the species completely independently or include in the fit as few other lines as possible. This allows us to explore a large parameter range with a simple fit. A joint fit of a whole band is much more complicated due to the many, often blended, lines in each band and only succeeds if the parameter range is limited sufficiently by the first run. We restrict the fit parameters in the second run to the 16th–84th percentile range of the respective parameter of the first run. In the third run, we fit for the excitation temperature of the temperature-sensitive species while keeping all other species fixed. This approach limits the degrees of freedom in each run to a manageable level.

The parameters we fit for are column density, linewidth, and line centroid. We fix the source size to unity, which means the source completely covers the beam, a reasonable estimate for slightly unresolved SSCs (L18). The species in our sample are typically detected with only a single line, so we have to assume an excitation temperature or infer it from the data. The latter cannot be done for all SSCs (see discussion in Section 4.5), so we fix $T_{rot} = 130$ K for the purely rotationally excited species and $T_{vib} = 300$ K for the rovibrational transitions. The former corresponds to the warm ISM component found by Mangum et al. (2013) and Gorski et al. (2017) on lower spatial resolution. Using this value, our analysis is consistent with L18, who used the same value. As it turns out (Section 4.5), the mean SO_2 rotational temperature of the SSCs where this measurement is possible is 127 K; hence, $T_{rot} = 130$ K is a good assumption. The assumption of $T_{vib} = 300$ K is an educated guess and supposedly on the lower side for an SSC environment (compared to less extreme Galactic hot cores as in Goldsmith et al. 1983; Wyrowski et al. 1999).

In the third run, we fit SO_2 and H_2CS for the most unstable parameter, the excitation temperature T_{rot}, in the range 25–1000 K. The detected SO_2 lines span a range in E_{lower} of ~40 K to >300 K, and the detected H_2CS lines cover $E_{lower} = 50$–770 K. Both species should therefore allow for an estimate of their excitation temperatures. Species other than these two do not cover a wide enough range in the energy states or detected lines for successful fits with free temperature parameters.

For our XCLASS fits, we find that an under-/overestimation in the fixed excitation temperature (T_{rot}, T_{vib}) causes over-/underestimation in column density by similar factors. Fitted column densities must thus be understood with a systematic error of the same order of the assumed excitation temperature (see discussion in Section 4.5). For the column density ratios of two species, this systematic effect affects both species similarly if the excitation temperature is equally under-/overestimated. Two species with similar excitation temperatures are therefore similarly over-/underestimated by the fixed T_{ex}, and the column density ratio is only weakly affected by the choice of T_{ex}. On the same note, relative comparisons between sources are meaningful if T_{ex} is similar between them.

3.3. Error Estimation

We estimate fit errors with a Monte Carlo scheme with 100 variations of the spectra to fit. For each variation, we add random draws of Gaussian noise to the observed spectra and thus sample the fit robustness against noise in the spectra, which is the dominant source of error. Errors are reported as the differences between the median and 16th (84th) percentiles[11] for lower (upper) error.

Details regarding the handling of blended lines, parameters, and parameter ranges (especially a discussion of the choice of T_{ex} and its implications), fit algorithms, and the Monte Carlo error estimation are described in Appendix A.

3.4. Derivation of Integrated Intensity

XCLASS does not offer the possibility to also report integrated intensity since it is built on physical instead of observational quantities. We therefore use the final XCLASS models to de-blend the spectra and derive integrated intensities for lines within the observed frequency range of the fitted species. This is done through Gaussian fits to the de-blended spectra. As such the integrated intensities inherit uncertainties due to blended lines and the Monte Carlo error estimation from the XCLASS fits.

3.5. Fitted Spectra

The observed spectra with the joint fit (third run) for all 14 SSCs in both sidebands are shown in Figure 1. Figure 2 provides an enlarged view of the spectra for SSC 14. The corresponding enlarged spectra for SSCs 1–13 can be found in Figure Set 2. In general, the model spectra fit the observed data well with only small deviations. Spectral ranges with many blended lines are less well fit than isolated bright lines, but the fit reliably disentangles the relative contribution of the species. The fit can deviate from the data slightly because XCLASS fits all lines of a species

[11] For Gaussian distributions, this range corresponds to $\pm 1\sigma$.

Table 2
Sample of the Parameters Fitted with XCLASS

SSC	Molecule	Vibration	Component	$\log N$ (cm^{-2})	σ ($km\ s^{-1}$)	μ ($km\ s^{-1}$)	T_{kin} (K)	τ_{int}
			(1)	(2)	(3)	(4)	(5)	(6)
1	CO	$\nu = 0$	0	17.85	40.0	−44.6	130	3.32
1	CO	$\nu = 0$	1	18.23	33.3	−22.1	130	7.89
1	CO	$\nu = 0$	2	18.24	29.0	20.3	130	8.08
1	CO	$\nu = 0$	3	17.39	30.0	68.7	130	1.15
1	CO	$\nu = 0$	4	17.68	39.6	106.2	130	2.22
1	HCO^+	$\nu = 0$	0	14.40	39.4	−34.3	130	1.50
1	HCO^+	$\nu = 0$	1	14.28	22.7	24.2	130	1.15
1	HCN	$\nu = 0$	0	14.62	37.4	−37.1	130	1.44
1	HCN	$\nu = 0$	1	14.38	20.5	24.6	130	0.82
1	HCN	$\nu_2 = 2$	0	16.29	31.9	−5.3	300	0.04
1	HCN	$\nu_2 = 1$	0	15.64	30.5	7.5	300	0.18
1	$H^{13}CN$	$\nu = 0$	0	13.59	20.3	−3.9	130	0.13
1	$H^{15}NC$	$\nu = 0$	0	13.37	18.1	10.0	130	0.07
1	CS	$\nu = 0$	0	14.53	33.9	−21.7	130	0.38
1	CS	$\nu = 0$	1	14.78	32.7	3.3	130	0.67
1	HC_3N	$\nu = 0$	0	14.66	50.0	−0.3	130	0.43
1	HC_3N	$\nu_6 = 1$	0	14.95	26.5	−0.7	300	0.05
1	SO	$\nu = 0$	0	15.04	21.6	8.8	130	0.51
1	$S^{18}O$	$\nu = 0$	0	14.85	48.6	9.9	130	0.14
1	SO_2	$\nu = 0$	0	15.52	35.1	1.9	84	3.53

Note. (1) The numbers assigned to the fitted components do not necessarily correspond to each other. (2) Molecular column density. (3) Velocity dispersion. (4) Line centroid position with respect to the systemic velocity of each SSC (see 2.2). (5) Kinetic temperature is fitted for SO_2 and H_2CS only and fixed to 130 K and 300 K for rotational and rovibrational species, respectively. (6) Total line opacity, i.e., integrated over the line. The typical column density error is 14.3% and consists primarily of uncertainty due to line crowding. Additionally, the systematic flux uncertainty applies with $\lesssim$5% for these observations according to the ALMA specifications.

(This table is available in its entirety in machine-readable form.)

simultaneously and respects the relations between lines. A particular line may thus be under-/overestimated if another line of the same species is found at lower/higher relative intensity. Some spectra, especially of the bright sources like SSC 14, show more spectral features than fitted, which will be studied in future work. The fits prove to provide robust parameter estimates as indicated by the Monte Carlo error estimation. Noise fluctuation and repetition of the fit only marginally affect the results. Hence, the dominant source of error is the flux calibration and continuum subtraction (only relevant in the USB for SSCs 2, 3, 4, 8, 13, and 14). Note that the LTE approximation used by XCLASS is also a severe source of uncertainty if the conditions in the SSCs are not close to LTE conditions.

4. Discussion

The ALMA data set allows us to study the ISM properties in the (proto-)SSCs in the core of a starburst. In the following, we focus on line ratios and selected properties for these objects.

4.1. Chemical Composition of the SSCs

Table 1 lists the detected lines with their integrated intensity for all 14 SSCs examined in this study. The corresponding parameters of the XCLASS model are given Table 2. SSC 14 is the most chemically rich proto-cluster in NGC 253, where we detect 19 species with 55 spectral lines. In SSC 2, 3, and 13, all species but $^{34}SO_2$ are detected. Only the bright species CO, HCN, HCO^+, and CS are detected in SSC 7, which is the poorest chemical repertoire detected in our sample. The vast differences in detection rate are affected by brightness: SSCs 5 and 14 are significantly brighter in HCN, HCO^+, and CS than the other SSCs, which are of comparable brightness in these lines. There is also an effect of intrinsic chemical richness and excitation environment as, e.g., SSCs 8–12 are located within ∼20 pc (projected) of each other and are comparable in total brightness in CS, HCN, and HCO^+ but differ significantly in the amount of detected species and spectral lines. SSC 14 is still the chemically richest SSC when considering its brightness. Even at 20% of its actual HCN or HCO^+ brightness (comparable to the HCN and HCO^+ total brightness of SSCs 1–4, 6–7, and 9–13), all species but ^{34}SO and the faint HC_3N^* would still be detected. The detected chemical richness of an SSC does not correlate with its location.

The 14 SSCs we study have been covered by Meier et al. (2015) in ALMA band 3 (86–115 GHz) observations at ∼50 pc resolution and overlap with the star-forming clumps identified by Ando et al. (2017) in ∼7 pc ALMA band 7 (340.2–343.4 GHz, 350.6–355.7 GHz, and 362.2–365.2 GHz) observations. They also correspond to the "super hot cores" identified by Rico-Villas et al. (2020) through their analysis of the HC_3N vibrationally excited emission, which we discuss in Section 4.4.1. Our results of the chemical richness of the SSCs are qualitatively consistent with these studies. A detailed comparison with Meier et al. (2015) proves difficult because their resolution of ∼50 pc is not high enough to resolve the SSCs and thus blends sources with varying chemical richness (e.g., their position 6 corresponds to SSCs 8–13). Ando et al. (2017) identify their clump 1 (corresponding to our SSC 14) as the most chemically rich clump, clumps 3 and 5 (SSCs 10+12 and 9) as the poorest, and clumps 2, 4, 6, 7, and 8 (SSCs 13, 8, 5, 4, and 2+3) as intermediate types. Our detection rates match that general picture; however, we place the SSCs corresponding to a few of the intermediate richness clumps toward higher or lower richness. Hence, high spatial resolution is

required to separate out sources of strongly varying chemical richness.

The detection fraction of species does not significantly correlate with the (integrated) intensity of one of the bright lines CO, HCN, HCO^+, and CS. Peak intensities as well as integrated intensities of the strongest component in CO are comparable within a factor of two among the SSCs. In CS, HCN, and HCO^+, peak intensity of the main component and also integrated intensity are correlated across lines. This might be due to CO tracing different gas than CS, HCN, and HCO^+ as expected from their different critical densities and tracer properties, or most likely CO is be optically thicker and saturated for all SSCs.

Especially in CO, but also in CS, HCN, and HCO^+, multiple components of similar peak intensity are present (SSCs 1, 2, 3, 5, 10, 11, and 12) while single components are detected in other species. This is already seen in the lower-resolution study by Ando et al. (2017) in their clumps 3 (SSCs 2 and 3) and 8 (SSCs 10 and 12). In SSCs 1, 2, 3, 10, and potentially SSC 4, the center of the dip between double peaks in CO, HCN, and HCO^+ coincides closely ($<5\,km\,s^{-1}$) with the peak position of other detected lines. Potential explanations are temperature gradients in the SSCs, self-absorption within the gas, or absorption against a background source. Similar absorption features are often seen in HCN and HCO^+ in Galactic molecular clumps and sometimes associated with inflow and outflow motions (e.g., Wyrowski et al. 2016). Very similar line profiles are seen in the Galactic Center proto-SSC Sgr B2 and attributed to self-absorption (Mills & Battersby 2017). In SSC 1 and 10, the potential absorption is strong and approaches zero in HCN and HCO^+. We note, however, that none of these features drops below zero in our continuum-subtracted spectra, which would be a clear indication of absorption into the continuum. These spectral features could also be interpreted structurally such that in CO, HCN, and HCO^+, we see layers of surrounding gas at higher/lower velocity whereas in the other molecules, we see the central region of the cloud. Absorption is more likely, though, especially when considering the lower critical densities and expected higher opacities of CO, HCN, and HCO^+ relative to the other species, which make CO, HCN, and HCO^+ more prone to being affected by absorption. It is still noteworthy that only SSCs 1, 2, 3, (4), and 10 show noticeable dip (absorption) features, although other sources are of similar or even higher brightness. If these spectral features are indeed caused by absorption, the reported intensities and column densities are underestimated. Derived ratios must then be considered limits (lower/upper depending on the ratio) in SSCs 1, 2, 3, and 10.

4.2. Dense Gas

HCN, HCO^+, and other molecules are often referred to as dense gas tracers, but it remains unclear what "dense gas" is and how well it is traced by these species. In the extragalactic community, HCN and HCO^+ transitions are typically considered to trace densities similar to their critical densities, and thus they are used to label molecular gas at $n > 10^5\,cm^{-3}$ as "dense". Historically, these species used to be among the few molecular species detectable in nearby galaxies due to their brightness. Newer studies in the Milky Way, however, show that HCN emission also arises from less dense regions down a few $100\,cm^{-3}$ and therefore well below the critical density (e.g., Shirley 2015; Kauffmann et al. 2017; Pety et al. 2017). In this section, we refer to HCN, HCO^+, HNC, and CS as dense gas tracers in the sense that they are tracers of molecular gas denser than that traced by CO.

Table 3 lists the line ratios of said dense gas tracers with each other and CO. The involved species are detected with multiple components, some of which deviate from the systemic velocity of the SSC inferred from less complex lines as discussed above. For table 3, we select the spectral component closest to said systemic velocity to focus on the SSCs instead of foreground (or background) emission. We do not show CO/HCO^+ because it is similar to CO/HCN as shown by the HCN/HCO^+ ratio.

4.2.1. Ratios with CO

Keeping in mind the aforementioned caveats about dense gas tracers, the ratios of HCN, HCO^+, and CS with CO translate to a proxy of the dense gas fraction (e.g., Gallagher et al. 2018). HCN most likely arises from gas with $n > 10^5\,cm^{-3}$, but can also be excited below these densities by infrared pumping or electron collisions (e.g., Jackson et al. 1995; Paglione et al. 1997; Knudsen et al. 2007). CS(7–6) has a critical density of $\sim 3 \times 10^7\,cm^{-3}$ and emits most effectively at $>60\,K$ thus tracing warm dense gas.

Both the CO/HCN and CO/CS ratios are lower than what has been found globally in, e.g., luminous infrared galaxies (LIRGs; Baan et al. 2008, CO(1–0)/HCN(1–0) = 12.5–100, CO(1–0)/CS(3–2) = 9–100), or a wide sample of galaxies (Gao & Solomon 2004). Gao & Solomon (2004) list CO(1–0)/HCN(1–0) = 17 on galaxy scales in NGC 253. Sakamoto et al. (2011) found CO(3–2)/HCN(4–3) = 12–17 in molecular complexes at $\sim$30 pc resolution. At a similar resolution of 32 pc, Meier et al. (2015) report CO(1–0)/HCN(1–0) of $\sim$6.0 to $\sim$10 across six locations in the central starburst disk.

Since we observe the higher *J*-transitions CO(3–2) and HCN (4–3) instead of the (1–0) transitions in the literature, the line ratios are not directly comparable until excitation has been considered. For the typical column densities, linewidths, and temperatures observed in our data, a simple estimation with the RADEX (van der Tak et al. 2007) radiative transfer code[12] suggests CO(3–2)/HCN(4–3) to be about twice the CO(1–0)/HCN(1–0) line ratio. Instead, we observe $\sim$1.5–2 times lower CO(3–2)/HCN(4–3) ratios compared to the Meier et al. (2015) CO(1–0)/HCN(1–0) and even lower relative to other literature values. The difference between our line ratios and the literature therefore cannot be explained by the higher excitation state of the lines observed here. Instead, the difference must be caused by selection and/or density effects. This may be due to the fact that we select on regions of actively star-forming dense gas while the resolutions of previous studies yield GMC scale averages.

The very low CO/HCN and CO/CS ratios in SSC 5 are noteworthy. The peak intensity differs by a factor of $\sim$1.5 but the linewidth of the main component appears much more narrow in CO, so both end up at similar integrated intensities. In this source, CO shows a wide distribution of peaks, some of which might be caused by absorption, whereas CS, HCN, and HCO^+ have only one peak very close to Gaussian in shape. The other CO components in SSC 5 do not contain relevant amounts of dense gas, apparently.

[12] Run using the online version at http://var.sron.nl/radex/radex.php.

Table 3
Dense Gas Fractions Specified by Line Intensity Ratios and Column Density Ratios

SSC	Line Intensity Ratio R_I				Column Density Ratio R_N			
	CO/HCN	CO/CS	HCN/HCO$^+$	CS/HCN	CO/HCN	CO/CS	HCN/HCO$^+$	CS/HCN
1	$4.9^{+0.2}_{-0.6}$	$10.1^{+9.3}_{-2.2}$	$1.0^{+0.1}_{-0.0}$	$0.5^{+0.1}_{-0.2}$	4100^{+190}_{-500}	2900^{+2700}_{-650}	$1.7^{+0.1}_{-0.0}$	$1.4^{+0.4}_{-0.7}$
2	$3.3^{+0.8}_{-0.9}$	$9.0^{+9.1}_{-3.9}$	$1.0^{+0.0}_{-0.0}$	$0.4^{+0.2}_{-0.2}$	2700^{+650}_{-710}	2600^{+2300}_{-1200}	$1.7^{+0.1}_{-0.1}$	$1.1^{+0.7}_{-0.5}$
3	$4.0^{+0.1}_{-0.1}$	$14.5^{+1.5}_{-1.4}$	$0.9^{+0.1}_{-0.0}$	$0.3^{+0.0}_{-0.0}$	3300^{+140}_{-72}	4100^{+430}_{-380}	$1.5^{+0.1}_{-0.0}$	$0.8^{+0.1}_{-0.1}$
4	$8.0^{+1.4}_{-1.8}$	$12.5^{+0.8}_{-2.5}$	$0.9^{+0.2}_{-0.3}$	$0.6^{+0.1}_{-0.1}$	7700^{+1300}_{-2000}	4200^{+270}_{-520}	$1.6^{+0.4}_{-0.4}$	$1.9^{+0.3}_{-0.3}$
5	$0.9^{+0.0}_{-0.0}$	$1.4^{+0.0}_{-0.0}$	$0.9^{+0.0}_{-0.0}$	$0.7^{+0.0}_{-0.0}$	760^{+9}_{-17}	400^{+4}_{-7}	$1.5^{+0.0}_{-0.0}$	$1.9^{+0.0}_{-0.0}$
6	$3.4^{+0.2}_{-0.3}$	$29.1^{+3.2}_{-2.4}$	$1.6^{+0.3}_{-0.2}$	$0.1^{+0.0}_{-0.0}$	2900^{+150}_{-260}	8700^{+1000}_{-780}	$2.8^{+0.6}_{-0.3}$	$0.3^{+0.0}_{-0.0}$
7	$12.7^{+2.5}_{-2.8}$	$26.1^{+4.7}_{-2.1}$	$0.5^{+0.3}_{-0.1}$	$0.5^{+0.1}_{-0.2}$	11000^{+2200}_{-2300}	7400^{+1200}_{-630}	$0.8^{+0.5}_{-0.2}$	$1.4^{+0.3}_{-0.5}$
8	$4.5^{+7.6}_{-1.2}$	$5.5^{+0.1}_{-0.1}$	$0.9^{+0.6}_{-0.5}$	$0.8^{+1.4}_{-0.2}$	4500^{+7500}_{-1300}	1900^{+41}_{-42}	$1.6^{+1.1}_{-0.8}$	$2.4^{+3.7}_{-0.7}$
9	$5.5^{+4.4}_{-1.7}$	$8.5^{+0.9}_{-1.5}$	$0.6^{+0.4}_{-0.2}$	$0.6^{+0.7}_{-0.2}$	5000^{+4300}_{-1600}	2700^{+320}_{-460}	$1.1^{+0.7}_{-0.4}$	$1.8^{+2.1}_{-0.5}$
10	$4.0^{+0.6}_{-1.6}$	$11.9^{+9.2}_{-4.6}$	$0.8^{+0.0}_{-0.0}$	$0.3^{+0.1}_{-0.2}$	3700^{+360}_{-1700}	3600^{+2600}_{-1600}	$1.4^{+0.0}_{-0.0}$	$1.0^{+0.2}_{-0.5}$
11	$5.0^{+4.9}_{-1.8}$	$5.9^{+1.9}_{-1.1}$	$0.8^{+0.5}_{-0.4}$	$0.8^{+0.7}_{-0.3}$	4600^{+4700}_{-1800}	1800^{+620}_{-440}	$1.4^{+0.8}_{-0.6}$	$2.5^{+2.1}_{-0.9}$
12	$6.3^{+1.0}_{-2.3}$	$7.8^{+1.2}_{-2.9}$	$1.1^{+0.1}_{-0.1}$	$0.8^{+0.0}_{-0.0}$	5700^{+990}_{-2400}	2400^{+430}_{-1000}	$1.9^{+0.1}_{-0.1}$	$2.4^{+0.1}_{-0.1}$
13	$9.3^{+1.4}_{-5.1}$	$11.4^{+6.6}_{-5.4}$	$0.7^{+0.4}_{-0.2}$	$0.7^{+0.3}_{-0.3}$	8400^{+1200}_{-3100}	3500^{+2000}_{-1800}	$1.2^{+0.7}_{-0.3}$	$2.0^{+0.9}_{-0.8}$
14	$2.3^{+0.0}_{-0.1}$	$2.6^{+0.2}_{-0.1}$	$0.9^{+0.0}_{-0.0}$	$0.9^{+0.0}_{-0.1}$	2400^{+48}_{-74}	960^{+68}_{-30}	$1.6^{+0.0}_{-0.0}$	$2.5^{+0.1}_{-0.2}$

Note. The ratios above are derived from the following rotational transitions: CO(3–2), HCN(4–3), HCO$^+$(4–3), and CS(7–6). Errors of 0.0 are due to rounding. The line intensity ratios R_I are derived from Gaussian fitting as explained in Section 3.4 while the column density ratios R_N result directly from XCLASS (see Section 3.2 for details).

Similar issues must be kept in mind for the other SSCs. We try to fit the component matching the other species most closely in velocity, but this assumption may not be exactly valid because of the unknown influence of absorption. Due to these effects, we caution against overinterpreting the line ratios involving CO and to a lesser degree also CS, HCN, and HCO$^+$. Depending on the unknown strength and frequency of absorption, sources may be affected to varying degrees.

4.2.2. HCN/HCO$^+$

The HCN/HCO$^+$ line ratio is proposed to differentiate starbursts from active galactic nuclei (AGNs) on an empirical basis (Kohno et al. 2001; Krips et al. 2008). The theoretical background of this tracer property is not yet clear but probably related to high temperatures and/or mechanical heating (Aalto et al. 2012; Izumi et al. 2013). Seyferts usually show HCN/HCO$^+$ > 1 while starbursts often have ratios $\lesssim$1 due to HCO$^+$ enhancement by PDRs (Kohno et al. 2001; Krips et al. 2008; Imanishi et al. 2009; Izumi et al. 2013, 2016; Martin et al. 2015; Meier et al. 2015; Privon et al. 2015; Imanishi et al. 2016). Exceptions to the usually good diagnostic power of HCN/HCO$^+$ are known in the literature (e.g., Privon et al. 2015).

The HCN/HCO$^+$ line ratios in all 14 SSCs are close to unity and thus within the transition regime between AGNs and starbursts. SSC 6 is the only source with a ratio significantly greater than unity whereas all other sources have ratios below or consistent with unity. Any hypothetical contribution of a highly obscured AGN should appear in the SSCs near the stellar kinematic center (α, $\delta = 00^h47^m33\overset{s}{.}134$, $-25°17'19\overset{''}{.}68$; Müller-Sánchez et al. 2010) and the continuum source TH2 (α, $\delta = 00^h47^m31\overset{s}{.}2$, $-25°17'17''$; Ulvestad & Antonucci 1997) proposed to be an AGN, both of which are close to SSCs 8–12. Signs of AGN activity have not been detected in NGC 253, and SSC 6 is located ∼50 pc (projected) from the kinematic center, so this cannot explain the slightly enhanced ratio. NGC 253 or at least the SSCs within the starburst are hence an exception to the aforementioned tracer properties of the HCN/HCO$^+$ ratio. If the HCN/HCO$^+$ intensity ratio reflects the abundance ratio, HCN/HCO$^+$ ~ 1 would indicate that HCO$^+$ is not (yet) enhanced as some studies suggest for a starburst environment (e.g., Krips et al. 2008). Potentially, the SSCs are still too young to have enhanced the HCO$^+$ abundance in PDRs through feedback. Following this line of argument, the SSCs must be either too young to have developed PDRs, or the PDR is still embedded in the cluster and does not affect the observable gas at the outer shells of the cloud (see opacity discussion below and in Section 4.3).

Line ratios of the order of unity are also expected if both lines are subject to significant opacity and thermalized. As discussed in Section 4.3, opacities in HCN are high at $\tau \gtrsim 1$, and similar values are expected for HCO$^+$ in the same source. The measured line ratios are therefore most likely set by opacity effects rather than abundance variations.

On larger scales, HCN/HCO$^+$ ~ 1 has been previously found. Meier et al. (2015) report HCN/HCO$^+$ ~ 1.1 for 10 regions across the Central Molecular Zone (CMZ), and Knudsen et al. (2007) and Jiménez-Donaire et al. (2017) find HCN/HCO$^+$ $= 1.1 \pm 0.2$ (1.1 ± 0.1, respectively) over the central region of NGC 253. The combined HCN (HCO$^+$) intensity of the SSCs amounts to only 0.15% (0.13%) of the total HCN (HCO$^+$) reported in Knudsen et al. (2007) in the 4–3 state. This means the galactic ratios are not dominated or influenced to a relevant degree by emission associated with the SSCs. Therefore, the SSCs do not deviate significantly from their large-scale surrounding in terms of their HCN/HCO+ line ratio.

4.2.3. CS/HCN

The CS/HCN ratio was proposed as a potential starburst/AGN tracer by tracing PDR/XDR environments where enhanced CS/HCN corresponds to XDR conditions (Meijerink et al. 2007; Izumi et al. 2013, 2016). Meier & Turner (2005) suggest that CS is a PDR tracer because it is better correlated with other known molecular PDR tracers (C_2H).

Table 4
Line Intensity Ratios of Selected Species

SSC	$HC^{15}N/H^{15}NC$	$HCN/H^{13}CN$	$HCN/HC^{15}N$	$SO/S^{18}O$	HCN/HC_3N	SO/SO_2	CS/SO_2
1	…	$6.4^{+1.5}_{-1.0}$	…	$1.7^{+0.8}_{-0.3}$	$3.5^{+0.8}_{-0.7}$	$1.7^{+0.3}_{-0.2}$	$5.0^{+1.6}_{-2.6}$
2	$1.5^{+0.5}_{-0.3}$	$13.5^{+0.9}_{-1.6}$	$11.8^{+1.3}_{-1.9}$	$14.2^{+1.5}_{-7.9}$	$5.5^{+1.1}_{-0.5}$	$2.3^{+0.1}_{-0.1}$	$3.9^{+2.3}_{-1.9}$
3	$1.6^{+0.5}_{-0.5}$	$6.8^{+0.4}_{-0.3}$	$5.5^{+1.6}_{-0.8}$	1218^{+78}_{-99}	$4.0^{+0.5}_{-0.3}$	$1.4^{+0.1}_{-0.1}$	$1.6^{+0.4}_{-0.3}$
4	…	$17.0^{+4.5}_{-7.0}$	$10.3^{+3.6}_{-3.9}$	$8.5^{+4.7}_{-3.2}$	$2.9^{+0.8}_{-1.3}$	$1.5^{+0.1}_{-0.2}$	$3.5^{+0.3}_{-0.3}$
5	$2.3^{+0.1}_{-0.2}$	$6.0^{+0.2}_{-0.2}$	$13.4^{+0.7}_{-0.9}$	$67.2^{+2.4}_{-17.6}$	$9.9^{+0.5}_{-0.4}$	$4.4^{+0.2}_{-0.2}$	$14.6^{+0.5}_{-0.4}$
6	…	$30.5^{+6.1}_{-3.7}$	…	…	…	…	…
7	…	…	…	…	…	…	…
8	$3.0^{+0.8}_{-0.6}$	$3.2^{+2.1}_{-2.2}$	$6.9^{+5.0}_{-4.6}$	$15.8^{+6.9}_{-5.3}$	$3.9^{+3.2}_{-2.4}$	$4.9^{+0.3}_{-0.4}$	$11.1^{+0.5}_{-0.7}$
9	…	$7.7^{+3.8}_{-3.2}$	…	…	…	…	…
10	…	$66.0^{+2.3}_{-9.1}$	…	…	$13.3^{+3.9}_{-2.7}$	$3.0^{+0.6}_{-0.5}$	$8.6^{+2.6}_{-3.7}$
11	…	$6.2^{+4.1}_{-3.1}$	…	…	$5.9^{+3.4}_{-2.6}$	$6.3^{+1.6}_{-1.4}$	$26.9^{+6.6}_{-5.5}$
12	…	$9.7^{+1.5}_{-1.3}$	…	…	…	$1.5^{+0.5}_{-0.3}$	$15.1^{+1.3}_{-1.8}$
13	$3.4^{+1.3}_{-1.6}$	$3.2^{+0.5}_{-0.5}$	$3.0^{+0.6}_{-0.6}$	499^{+128}_{-57}	$2.1^{+0.3}_{-0.3}$	$2.6^{+0.1}_{-0.1}$	$2.6^{+0.8}_{-0.7}$
14	$4.0^{+0.5}_{-0.5}$	$3.5^{+0.1}_{-0.1}$	$4.5^{+0.2}_{-0.2}$	$94.1^{+108}_{-42.5}$	$3.0^{+0.1}_{-0.1}$	$4.3^{+0.3}_{-0.1}$	$8.1^{+0.6}_{-0.6}$

Note. The ratios above are derived from the following rotational transitions: HCN(4–3), $H^{13}CN$(4–3), $HC^{15}N$(4–3), $H^{15}NC$(4–3), HC_3N(38–37), CS(7–6), $SO(8_8–7_7)$, $S^{18}O$ $(8_9–7_8)$, and $SO_2(11_{4,8}–11_{3,9})$.

In NGC 253, the CS/HCN ratio scatters significantly across SSCs and does not correlate with the other dense gas tracer ratios in Table 3. It seems to correlate with the chemical richness, expressed as the number of detected species, in an SSC. There are no significant correlations between CS/HCN and SSC properties listed by L18 (virial mass, gas mass, stellar mass, surface and volume density, freefall time, and pressure). According to the mentioned PDR/XDR models by Meijerink et al. (2007) and Izumi et al. (2013, 2016), the obtained CS/HCN ratios are consistent with PDR chemistry under the reasonable assumption that the density of the emitting gas is within factors of a few of 10^5 cm^{-3}. For XDR chemistry, CS/HCN > 1 would be expected.

4.2.4. HCN/HNC

HCN/HNC < 1 is usually a sign of cold (10–20 K) dark clouds but can also occur through mid-IR pumping and XDRs in (U)LIRGs, starbursts, or active galaxies (e.g., Schilke et al. 1992; Aalto et al. 2007b; Baan et al. 2008). Some (U)LIRGS show bright HNC where the HNC might even be brighter than HCN (Huettemeister et al. 1995; Aalto et al. 2002; Aladro et al. 2015). Such low HCN/HNC ratios are possible through chemical reactions at moderate temperatures and densities, infrared pumping, but also high optical depth in HCN (Aalto et al. 2002). Graninger et al. (2014) argue that HNC and HCN have great potential as temperature tracers because the formation and destruction paths are temperature dependent with increasing HCN/HNC for increasing temperature. This line ratio can also be a proxy for the evolutionary stage on a starburst where HCN/HNC $\gg 1$ indicates shock-dominated regions common in early starbursts (Aladro et al. 2015). Loenen et al. (2008) show a PDR/XDR model and show that the HCN/HNC line ratio can differentiate between PDR and XDR. In the case of PDRs, this model can further discern between density regimes based on the HCN/HCO^+ ratio. There seems to be no final consensus about the tracer properties of the HCN/HNC ratio in the literature. It seems likely, however, that this ratio is related to PDR/XDR chemistry.

Table 4 lists the line ratios of HCN and its isomer HNC. This ratio is measured in the ^{15}N species and is thus less affected by optical depth effects (see Section 4.3). The line ratios in SSC 2 and 3 are almost consistent with unity while the SSCs 5, 8, 13, and 14 are significantly higher at ∼2–4. In the literature, $H^{13}CN/HN^{13}C \sim 2.5$ is reported for 10 ∼2″ regions across the center of NGC 253 (Meier et al. 2015), which should be comparable to first order since both ^{13}C and ^{15}N are significantly less abundant than the main isotopologues. SSCs 5, 8, 13, and 14 are thus similar in $HC^{15}N/H^{15}NC$ to the large-scale ratio while SSC 2 and 3 deviate toward lower ratios.

The generally low ratios in SSC 2 and 3, and to a lesser degree also in SSC 5, 8, 13, and 14 might be explained by radiative pumping. This is further substantiated by the detection of vibrationally excited HCN in these sources, which is excited via infrared pumping (see Section 4.4.3). In the model of Graninger et al. (2014), the observed HCN/HNC ratios imply temperatures <35 K, which are unlikely in a starbursting environment (also see Section 4.5 on temperature measurements).[13] In the Loenen et al. (2008) model, the measured HCN/HNC implies that none of the SSCs contain an XDR, but all are characterized by PDR chemistry at $n \sim 10^5$ cm^{-3}, as we discuss in Section 4.2.5.

4.2.5. SSC Energy Source

Loenen et al. (2008) and Baan et al. (2008) proposed diagnostic diagrams to infer the excitation environment in the nuclear regions of galaxies. They list different regimes for line ratios and column density ratios of HCN, HCO^+, HNC, and CS related to PDR/XDR chemistry. These are based on PDR/XDR models by Meijerink & Spaans (2005) and Meijerink et al. (2006, 2007) with the assumption of steady-state chemistry.

We use these diagnostics to infer the probable excitation mechanisms in the SSCs. Figure 3 shows the relevant column density ratios of HCN, HCO^+, and HNC. $H^{14}NC$ (4–3) at 362.63 GHz falls outside our observed band, but we can correct the detected $H^{15}NC$ using the $^{14}N/^{15}N$ isotope ratio obtained from HCN and $HC^{15}N$. The SSCs where all necessary lines are detected

[13] If the reaction barrier of 200 K is used. Their alternative model with a 1200 K reaction barrier does not show a temperature dependence of the HCN/HNC ratio.

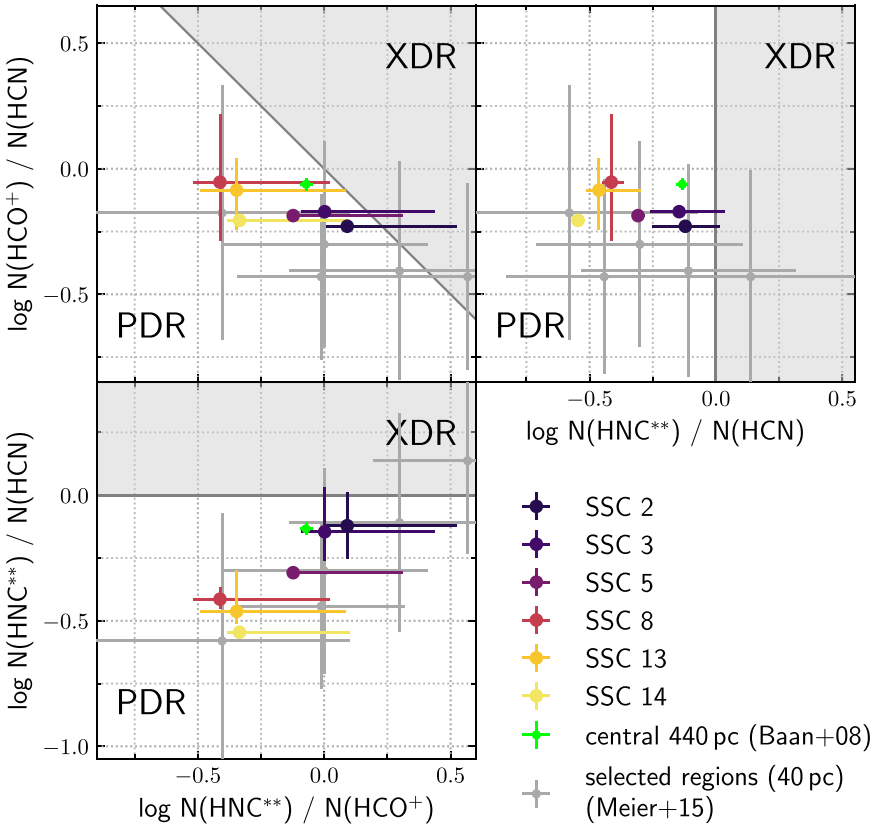

Figure 3. PDR–XDR chart according to Loenen et al. (2008) and Baan et al. (2008) for ratios of HCN, HCO^+, and HNC column densities. In our observations, we do not observe $H^{14}NC$ but $H^{15}NC$, so we estimate $H^{14}NC$ using the isotope ratio $^{14}N/^{15}N$ derived from $H^{14}NC$ and $H^{15}NC$ of each SSC. In the plot, this is marked by the ** symbol. The correction is possible for only six out of the 14 SSCs due to the detection rate of $H^{15}NC$. The Baan et al. (2008) estimate for the central region (26″, 440 pc) of NGC 253 extends over all SSCs and surrounding gas. The 40 pc (2.″4) regions of Meier et al. (2015) focus on selected positions within NGC 253 and also cover the SSCs. However, they are derived from the respective (1–0) transitions.

(SSCs 2, 3, 5, 8, 13, and 14) all fall in the PDR regime of the model. SSCs 2 and 3 are barely compatible with XDR conditions within 1σ errors. For PDRs, the HCO^+/HCN ratio can allow us to differentiate density regimes (Loenen et al. 2008) where the measured $\log(HCO^+/HCN) \sim 0$ indicates volume density $n \sim 10^5\,cm^{-3}$. Baan et al. (2008) further utilize CS/HCN as a column density tracer with CS/HCN $\geqslant 1$ at $N_H \gtrsim 10^{22}\,cm^{-2}$ and CS/HCN $\leqslant 1$ for lower column densities. In the SSCs 2, 3, 5, 8, 13, and 14 that we can relate to PDRs, the line ratio CS/HCN < 1 in all cases, implying high column densities $>10^{22}\,cm^{-2}$ as are expected for this high-mass, dense environment. The H_2 column density derived from the CO intensity in Table 1 (using $X_{CO} = 0.5 \times 10^{20}\,cm^{-2}\,(K\,km\,s^{-1})^{-1}$; Paglione et al. 2001; Leroy et al. 2015) is indeed between $\sim 5.1 \times 10^{22}\,cm^{-2}$ (SSC 5) and $\sim 2.7 \times 10^{23}\,cm^{-2}$ (SSC 14).

Figure 3 also shows the ratios obtained by Baan et al. (2008) for the (3–2) transitions of the involved species. Their results, from single dish observations, cover the central 26″ (~440 pc) and thus average all SSCs and further nuclear molecular gas. Reassuringly, their position for NGC 253 in the diagnostic diagrams is close to the average of our detected SSCs. The $\lesssim$0.2 dex mismatch is not significant but, if real, most likely caused by the nuclear gas outside the SSCs. Our measurements are furthermore consistent with Meier et al. (2015) who report the (1–0) transitions of HCN, HNC, and HCO^+ for 10 selected regions of 2.″4 (~40 pc). Since they, too, do not observe HNC directly, we infer the HNC column density and line intensity from $HN^{13}C$ and the $^{12/13}C$ ratio obtained from $H^{12}CN$ and $H^{13}CN$. Note that Meier et al. (2015) estimate their column densities assuming optically thin LTE conditions whereas we consider optical depth.

As a consistency check, we also construct Figure 3 with observational (instead of modeled) data using the line intensity ratios and find the same qualitative result of chemistry consistent with a PDR environment. Details are discussed in Appendix B.

Finding PDR chemistry in the SSCs on parsec scales is consistent with the large-scale study by Martín et al. (2009) who confirm a photo-dominated chemistry for their detected typical PDR tracers in the central 400–500 pc of NGC 253.

Obviously, the two PDR/XDR models discussed in Section 4.2.3 and here cannot simultaneously apply as they attribute different tracer properties to CS/HCN. However, it is reassuring that both models consistently favor PDR conditions in all SSCs. For embedded (proto-)SSCs, PDR-dominated chemistry is expected, although large amounts of young O/B-stars could potentially emit enough short-wavelength radiation to create a mild XDR. As mentioned before, SSCs 8–12 are located close (<0.″5, <8.5 pc) in projection to the stellar kinematic center (α, $\delta = 00^h47^m13\overset{s}{.}179$, $-25°17'17\overset{''}{.}13$; Müller-Sánchez et al. 2010) and the continuum source TH2 (α, $\delta = 00^h47^m31\overset{s}{.}2$, $-25°\ 17'\ 17''$; Ulvestad & Antonucci 1997) proposed to be an AGN. At this location, they could be influenced by a potential AGN that may exhibit XDR properties. NGC 253 hosts a supermassive black hole (SMBH) of $\sim 8 \times 10^6\ M_\odot$ (Rodríguez-Rico et al. 2006; Davis et al. 2014) but shows no clear sign of even a low-luminosity AGN (Müller-Sánchez et al. 2010; Günthardt et al. 2015). XDR chemistry in nearby SSCs could provide hints toward

a low-luminosity, obscured AGN. As discussed above, both models at hand, however, exclude this possibility.

Finally, it must be noted that our finding that all SSCs (where possible) are consistent with PDR chemistry suggests that X-rays are not the main source of energy input. It does not imply the inverse, that UV heating is the dominant energy input. Mechanical heating from, e.g., shocks associated with accretion or outflows can dominate the energy budget while UV radiation only contributes. In fact, Martin et al. (2006) detect typical PDR tracers in the central 200 pc of NGC 253 but conclude that the heating is dominated by large-scale low-velocity shocks as they show by comparing NGC 253 to other starbursts and the Galactic center. This tension was solved by Meier et al. (2015; see their Figure 10) who could spatially separate energy sources in early ALMA observations at 3″ (∼50 pc) resolution. They draw a picture of an inner nuclear disk (where the SSCs are located) dominated by PDRs but with a contribution of widespread shocks. The inner nuclear disk is surrounded by an outer nuclear disk in which shocks dominate similar to bar shock regions in other galaxies. This picture is consistent with the new data presented here.

4.3. Isotopic Ratios and Optical Depth

Table 4 lists line ratios of the HCN isotopologues $H^{13}CN$ and $HC^{15}N$ with HCN. As the isotopologues are less abundant and therefore less bright and less optically thick, such a line ratio can act as a proxy for the optical depth. Although XCLASS fits for opacity, we here follow the classic approach and estimate it from line ratios. We find that the opacities fitted by XCLASS are often highly uncertain and strongly influenced by, e.g., noise spikes or (partially) blended lines. Therefore, classical line ratios provide a more robust estimate of opacities.

We detect $HCN/H^{13}CN$ with a large spread of approximately one order of magnitude in the range 3.2–66. In $HCN/HC^{15}N$, the ratios scatter less between 3.0–11.8. Both line ratios show a similar pattern with low ratios in SSCs 13 and 14, intermediate ratios in SSCs 3, and high ratios in SSC 2 and 4. In SSCs 5 and 8, the $HCN/H^{13}CN$ ratios are significantly lower than $HCN/HC^{15}N$ considering the relative range of ratios observed.

Our $HCN/H^{13}CN$ ratios scatter around the respective large-scale ratios in the center of NGC 253 with a bias toward lower ratios. Jiménez-Donaire et al. (2017) found $HCN/H^{13}CN = 17 \pm 1$, and Meier et al. (2015) obtained $HCN/H^{13}CN = 10$–15. Both studies cover the entire center of NGC 253 at 170 pc (single aperture) and 35 pc (probing 10 regions) resolution, respectively, whereas we focus on the SSCs at parsec scales.

In the simplest case where HCN is optically thick, $H^{13}CN$ is optically thin, and the gas is perfectly mixed at a constant density, the optical depth

$$\tau^{^{13}C} = T_b^{^{13}C} / T_b^{^{12}C} \quad (1)$$

depends on the observed intensity ratio and

$$\tau^{^{12}C} = \tau^{^{13}C} \times [^{12}C]/[^{13}C] \quad (2)$$

follows from the abundance ratio (e.g., Jiménez-Donaire et al. 2017). Further assumptions are equal beam filling factors and a common excitation temperature for both isotopologues. The same arguments apply to $HC^{15}N$ and $S^{18}O$. This simple model of optically thick main species and optically thin isotopologues is often assumed in nearby galaxies. Given the dense and compact SSCs, it provides an estimate of optical depth but may not be exactly valid.

For the abundance ratios $^{12/13}C = [^{12}C]/[^{13}C]$, $^{14/15}N = [^{14}N]/[^{15}N]$, and $^{16/18}O = [^{16}O]/[^{18}O]$, we turn to the literature to break the degeneracy of optical depth and abundance ratio. We adopt $^{12/13}C = 40 \pm 20$ (among nearby galaxies including NGC 253; Martin et al. 2010, 2019; Henkel et al. 2014; Tang et al. 2019), $^{14/15}N = 200 \pm 1$ dex (Viti et al. 2019, and references therein, see Table 1 for an overview), and $^{16/18}O = 130 \pm 40$ (NGC 253; Martin et al. 2019).

With the arguments above, we obtain $\tau_{H^{13}CN} = 0.05 - 0.3$ and $\tau_{HCN} = 2.0$–12. SSCs 1, 3, 5, 8, 9, 11, 13, and 14 would have quite high optical depths in the ^{12}C ($\tau_{H^{12}CN} > 5$) as well as the ^{13}C lines ($\tau_{H^{13}CN} \gtrsim 0.15$) while in the other SSCs, $\tau_{H^{12}CN} \sim 1 - 5$ are moderately thick. SSC 10 with $\tau_{H^{12}CN} \sim 0.6$ is marginally optically thick. For the $^{14/15}N$ ratio, $\tau_{HC^{15}N} = 0.08 - 0.3$ or $\tau_{HC^{14}N} = 15 - 66$. In ^{16}O and ^{18}O derived from SO, we obtain $\tau_{S^{18}O} < 0.1$ and $\tau_{S^{16}O} \lesssim 15$. A very low ratio in SSC 1 and corresponding high opacity ($\tau_{S^{18}O} = 0.6$, $\tau_{S^{16}O} = 78$) likely originate from confusion between the $S^{18}O$ and HC_3N lines.

In order to match the two estimates for τ_{HCN}, $^{12/13}C$ on the high side and $^{14/15}N$ on the low side of extragalactic measurements would be required. Jiménez-Donaire et al. (2017) estimate the optical depth at $\tau_{H^{12}CN} = 2.5$ and $\tau_{H^{13}CN} = 0.07$ averaged over the whole center of NGC 253. The HCN opacities of SSCs 2, 4, 6, and 12 do not stand out above this large-scale environment, while the other SSCs show higher optical depths in HCN. As indicated above, this trend in optical depth correlates with cluster age (see Section 4.4).

Given the high optical depths measured for some species, it must be noted that different species do not have to originate from the same location in the SSC cloud. If the gas density is not constant, emission from the more optically thick line originates from outer layers of the cloud. Chemical variations may thus be reflected in one line but not the other in all line ratios of this study. For instance, chemical enrichment by stellar winds of young stars within the forming cluster may affect only the inner regions of the SSC parent cloud.

4.4. Other Lines

We detect a multitude of molecular species and spectral lines in these deep observations. In the following section, we focus on a few of them.

4.4.1. HC_3N

HC_3N is a tracer for warm and dense gas (e.g., Tanaka et al. 2018). It has multiple bending modes (ν_5, ν_6, ν_7) at IR frequencies, which makes it sensitive to a strong IR field and allows HC_3N to act as a hot dust tracer when IR cannot be observed directly due to extinction (Rico-Villas et al. 2020). UV radiation and CRs can easily destroy the molecule, so it traces shielded IR irradiated dense gas (e.g., Costagliola & Aalto 2010). HC_3N abundances are enhanced in hot environments due to evaporation from dust grain mantles. Galactic detections are thus typically in hot cores (e.g., Sgr B2; de Vicente et al. 2000), but HC_3N was also detected in other galaxies, such as NGC 253, NGC 4418, and IC 342 (e.g., Meier & Turner 2005; Aalto et al. 2007a; Aladro et al. 2011; Costagliola et al. 2011; Meier et al. 2011). Most often the 10–9 transition at ∼90 GHz is detected (e.g., Costagliola et al. 2011), but detections up to $J_{upper} > 30$ are given in the literature as

well as detection of the vibrational states (ν_6,ν_7; e.g., Costagliola & Aalto 2010; Costagliola et al. 2011; Martin et al. 2011).

HC_3N lines are often the brightest, or at least among the brightest, lines after CO, HCN, HCO^+, and CS in our spectral window. This directly implies a high IR radiation field, because due to their high critical densities ($>10^8\,cm^{-3}$), HC_3N transitions cannot be purely collisionally excited; they also need to be pumped in the IR. Furthermore, we detect the (38–37) and (39–38) lines, so the temperatures must be high in order to excite these transitions (see Section 4.5). The ubiquitous, highly excited HC_3N and the observation that many SSCs contain PDRs (Section 4.2) pose constraints on the PDR or the dense gas geometry. High UV fluxes in a PDR can quickly dissociate HC_3N. Therefore, the UV field illuminating the PDRs must be either weak, or the HC_3N is well shielded from the photodissociating radiation, or alternatively the HC_3N emission is spatially separate from the PDRs. As discussed in Section 4.2.5, the PDR versus XDR discrimination only indicates the relative, not the absolute strength and does not cover mechanical heating as an energy source. In this context, the observation of bright HC_3N implies a weak PDR and dominant mechanical heating likely by gas accretion onto the forming SSCs and proto-stellar outflows. On the other hand, if the HC_3N and the PDR gas traced by the $HCN/HCO^+/HNC$ emission are spatially separated, the PDR can either be driven from the inside by the SSC in the center of the surrounding molecular cloud or from the outside by neighboring sources in an outer shell of the cloud. The first case implies a radially stratified model of onion-like layers with $HCN/HCO^+/HNC$ in the inner irradiated region and an outer layer of HC_3N. In the second case, HC_3N is shielded inside the cloud from external radiation, but $HCN/HCO^+/HNC$ can be well mixed with HC_3N. Without additional tracers of mechanical heating and cloud structure, we currently cannot distinguish these possibilities. At much lower resolution and for the central 400–500 pc, Martín et al. (2009) show that the PDR tracers originate in the outer layers of UV-illuminated clouds, similar to the aforementioned onion-layer structure. Our study, however, focuses on particular sources at 200 times higher resolution, which may not share this large-scale structure.

The ratio of HCN over HC_3N might be interpreted as a "super dense gas" fraction or very high-density to high-density gas ratio. Such a ratio is, as all line ratios are, only meaningful if HCN and HC_3N originate from the same region. Under that assumption, HCN/HC_3N implies that the highest fraction of very dense gas can be found in SSC 13 whereas SSC 10 would contain little very high-density gas (see Table 4). Increasing HCN/HC_3N ratios should occur when a molecular cloud gets disrupted by feedback as HC_3N is dissociated before HCN, and even earlier the favorable conditions for IR pumping are shut down as the self-shielding of the cloud diminishes. Toward the end of a molecular cloud lifetime, increasing HCN/HC_3N should thus be an age tracer, and the evolutionary sequence would be 13, 4, 14, 1, 8, 3, 2 from young to old. Rico-Villas et al. (2020) recently dated[14] the super hot cores within the SSCs by the fraction of proto-stellar (inferred from the IR radiation field pumping the HC_3N vibrational transitions) to stellar luminosity (inferred from the ionizing luminosity), which results in an almost inverted sequence (2, 3, 13, 1, 8, 14, 4). This suggests that the HCN/HC_3N ratio is not a reliable age tracer, at least for the young, deeply embedded SSCs in this study. Potential causes of the mismatch are structural effects, i.e., HCN and HC_3N not originating from the same region, or that all of the SSCs are too young to cause detectable effects on the HCN/HC_3N ratio. The latter is supported by the fact that the oldest SSCs (zero-age main-sequence SSCs 6, 7, 9, 10, 11, and 12, according to Rico-Villas et al. 2020) are consistently found at higher HCN/HC_3N than the younger proto-SSCs (1, 2, 3, 4, 8, 13, and 14) by factors of ∼1–4.

HCN/HC_3N ratios of 3–4 are commonly reported in nearby galaxies on scales of hundreds of parsecs for low-J and high-*J* HC_3N lines (NGC 4418, IC 342; Meier & Turner 2005; Aalto et al. 2007a; Sakamoto et al. 2010; Meier et al. 2011). Apart from SSC 13, the other SSCs show considerably larger ratios than this nearby galaxy average. In the center of NGC 253, $HCN/HC_3N \sim 10$ has been measured by Lindberg et al. (2011) over 25″ (425 pc). Hence, HC_3N/HCN in the SSCs does deviate in both directions by factors of a few from the large-scale average.

The detection of vibrationally excited HC_3N is among the first extragalactic of such detections (Costagliola & Aalto 2010; Costagliola et al. 2011; Martin et al. 2011). It is especially noteworthy that we detect high-*J* vibrationally excited lines, which require high temperatures and a strong IR field. With these observations, we can confirm that HC_3N is associated with dense star-forming gas and a starbursting environment.

4.4.2. Sulfur Chemistry

Chemical studies suggest that the fractional abundance of CS is sensitive to both the abundances of sulfur and oxygen (Graedel et al. 1982). SO_2 is related to turbulent gas near stellar activity (Minh et al. 2016). In undisturbed gas, sulfur is thought to be depleted onto ice grain mantles, and sulfur-bearing species may act as chemical clocks in the evolution of SF. SO and SO_2 form from grain-evaporated H_2S, and abundances increase with time until at later times, most of the sulfur is captured in CS, H_2CS, and OCS (Hatchell et al. 1998). The SO/SO_2 ratio may act as a crude clock with lower ratios toward later times (Charnley 1997). SO_2 is also used as a tracer for low-velocity outflows in stellar cores (Wright et al. 1996; Liu et al. 2012).

SO/SO_2 and CS/SO_2 line ratios are given in Table 4 for the ground state of SO, CS(7–6), and SO_2 $11_{4,8}$–$11_{3,9}$. The SO/SO_2 ratios vary by a factor of ∼5 across SSCs and ∼7 in CS/SO_2. Both ratios follow the same trend, with low ratios in SSCs 1, 3, and 4, and the highest ratios in SSCs 5, 8, and 11. If SO/SO_2 relates to age, the former are older while the latter are younger. This sequence does not correlate with the HC_3N age dating and Rico-Villas et al. (2020).

Martin et al. (2005) studied the sulfur chemistry in NGC 253 at 200–500 pc resolution, which provides an average value for all SSCs and the surrounding gas. They find fractional abundances $CS/SO_2 = 5$ and $SO_2/SO = 1$, which are considerably lower than our average line ratios over the detected SSCs of $CS/SO_2 = 9.2$ and $SO_2/SO = 3.1$. It must be noted that Martin et al. (2005) observed less excited gas with transitions up to CS(5–4), SO($4_3 - 3_2$), and SO_2($8_{2,6} - 8_{1,7}$) whereas we cover transitions above those and up to CS(7–6), SO($8_8 - 7_7$), and SO_2($17_{4,14} - 17_{3,15}$). Therefore, excitation effects may shift the line ratios. Given the uncertainties, the

[14] Their method can only date SSCs with a significant fraction of proto-stellar contribution and thus age dating is possible only until the cluster reaches the zero-age main sequence.

enhanced ratios in the SSCs could be explained by a factor of two depletion of SO_2 or, more likely, factors of two to three enhancement of SO and CS relative to the large-scale average from Martin et al. (2005).

4.4.3. Vibrationally Excited Species

The vibrationally excited lines of HCN and HC_3N have high critical densities (e.g., HCN $\nu_2 = 1$, $l = 1f n_{\rm crit} > 10^{10}\,{\rm cm}^{-3}$), which make purely collisional excitation unlikely. Instead, radiative excitation, particularly in the IR, is required (e.g., at 14 μm for HCN $\nu_2 = 1$, $l = 1f$; Ziurys & Turner 1986). These vibrational lines have been frequently observed toward nuclei of nearby (U)LIRGs (Sakamoto et al. 2010, 2013; Aalto et al. 2015; Imanishi et al. 2016, 2017; Falstad et al. 2018) but also in Galactic hot cores (Rolffs et al. 2011a, 2011b, 2011c; Aalto et al. 2015). In buried galactic nuclei powered by AGNs or starbursts, the dust emission can become optically thick and very effectively pump vibrationally excited HCN and HC_3N lines, similarly to a greenhouse (e.g., González-Alfonso & Sakamoto 2019). However, no AGN, not even a low-luminosity AGN, has been found in NGC 253 yet (Müller-Sánchez et al. 2010; Günthardt et al. 2015).

For HCN and HC_3N, we detect vibrationally excited lines in six out of 14 SSCs for HCN^* ($\nu_2 = 1$, $\nu_2 = 2$) and eight out of 14 ($\nu_6 = 1$), eight out of 14 ($\nu_7 = 1$), and six out of 14 ($\nu_7 = 2$) for HC_3N^* (see Table 1), so we can estimate the fraction of rovibrational versus purely rotational excitation. The rovibrational lines are very crowded, however, and blend into compact blocks of emission in some SSCs. All vibrational bending modes (f and e) for each ν level are detected with one line only, which makes it difficult to disentangle the spectra. The theoretical relationship between vibrational modes within the same rovibrational species as implemented in XCLASS constrains the relative line strengths, but systematic effects might remain. Table 5 lists the rotational over rovibrational line ratios of the f bending modes. In HCN(4–3)$\nu_2 = 1$, $l = 1f$, we find line ratios of HCN/HCN^* typically in the range ∼1.5–8 where detected. This corresponds to vibrationally excited rotational state fractions of ∼10%–40%. The higher value of ∼16 in SSC 11 indicates close to negligible relative importance of vibrational excitation of only 5%. The higher HCN(4–3)$\nu_2 = 2$, $l = 1f$ state is negligible relative to HCN and HCN(4–3)$\nu_2 = 1$, $l = 1f$ according to the high intensity ratios of >8.

For HC_3N, vibrational excitation is a more important mechanism relative to purely rotational excitation: where detected, the line ratios between purely rotational and vibrationally excited variants are low, at typically ∼1–3 corresponding to fractional contributions of the vibrationally excited lines of 25%–50%. These high fractions of emission in vibrationally excited lines hint at strong IR (around ∼14 μm) fields in the SSCs. Such an IR environment can be expected for forming SSCs as they are still deeply embedded (L18) and undetected in optical and near-IR (Walter et al. 2017). Emission from the forming stars is still trapped inside the SSC due to high opacity and does not yet leak outside. L18 argue for high optical depths in the IR due to their detection of 350 GHz emission at $\tau \sim 0.1$, which implies $\tau = 5$–10 at the peak of the dust SED (20–30 μm). Such opacities are more than high enough to create the aforementioned conditions for 14 μm trapping and IR pumping.

Rico-Villas et al. (2020) recently investigated the super hot cores in the SSCs using HC_3N. Their spectral window partially overlaps with our setup, but we detect further vibrationally excited HC_3N lines as listed in Table 1. From our detections, we can confirm their observation that SSCs 6 and 7 lack HC_3N even in the ground state and SSCs 9, 10, and 12 do not show vibrationally excited HC_3N. However, we detect two HC_3N^* species in SSC 11. Qualitatively, our HC_3N detection rates confirm the conclusion of Rico-Villas et al. (2020) that SSCs 6, 7, 9, 10, 11, and 12 are older than SSCs 1, 2, 3, 4, 5, 8, 13, and 14.

Table 5
Integrated Intensity Rovibrational over Rotational Excitation Fraction for Selected HCN and HC_3N Lines

SSC	HCN/HCN^* $\nu_2 = 1$, $l = 1f$	HCN/HCN^* $\nu_2 = 2$, $l = 2f$	HC_3N/HC_3N^* $\nu_7 = 1$, $l = 1f$	HC_3N/HC_3N^* $\nu_7 = 2$, $l = 2f$
1	$3.7^{+0.5}_{-0.3}$	$30.1^{+15.4}_{-9.9}$	…	…
2	$5.7^{+0.3}_{-0.4}$	$28.6^{+3.9}_{-3.4}$	$1.6^{+0.2}_{-0.3}$	$2.1^{+0.3}_{-0.4}$
3	$3.1^{+0.3}_{-0.2}$	$24.2^{+8.6}_{-4.8}$	$1.1^{+0.2}_{-0.1}$	$3.1^{+0.9}_{-0.6}$
4	$2.9^{+0.7}_{-1.2}$	$8.4^{+2.4}_{-3.3}$	$2.9^{+0.8}_{-0.5}$	$3.1^{+0.8}_{-0.5}$
5	$7.9^{+0.1}_{-0.2}$	$81.4^{+13.6}_{-10.5}$	$2.2^{+0.1}_{-0.2}$	$5.1^{+1.0}_{-0.7}$
6	…	…	…	…
7	…	…	…	…
8	$2.7^{+1.8}_{-1.8}$	$58.7^{+50.6}_{-38.4}$	$2.2^{+1.0}_{-0.3}$	…
9	…	…	…	…
10	…	…	…	…
11	$16.2^{+9.3}_{-7.5}$	…	$6.1^{+1.4}_{-0.7}$	…
12	…	…	…	…
13	$1.4^{+0.2}_{-0.2}$	$9.7^{+1.6}_{-1.5}$	$1.4^{+0.1}_{-0.1}$	$2.2^{+0.2}_{-0.2}$
14	$2.0^{+0.1}_{-0.0}$	$17.0^{+2.4}_{-2.9}$	$1.9^{+0.1}_{-0.1}$	$4.8^{+0.2}_{-0.2}$

Note. The rovibrational line used for each respective ratio is given in the second row.

Table 6
Excitation Temperatures Obtained by XCLASS Fitting

SSC	H_2CS	SO_2
1	…	84^{+25}_{-14}
2	103^{+60}_{-23}	114^{+11}_{-14}
3	>242	91^{+13}_{-7}
4	>160	191^{+35}_{-32}
5	>237	134^{+20}_{-26}
6	…	…
7	…	…
8	248^{+166}_{-75}	129^{+11}_{-23}
9	…	…
10	…	47^{+72}_{-11}
11	…	…
12	…	…
13	>226	122^{+25}_{-21}
14	141^{+15}_{-16}	228^{+15}_{-20}

4.5. ISM Temperature

The rotational temperatures derived by XCLASS for H_2CS and SO_2 are given in Table 6 and also plotted in Figure 4 for comparison.

SO_2 is detected in only 11 out of 14 SSCs but confines the temperature to typically ±20 K (16th–84th percentiles) if detected. In SSCs 11 and 12, the SO_2 lines are detected but do not allow for a robust temperature estimation as the signal-to-noise ratio is too

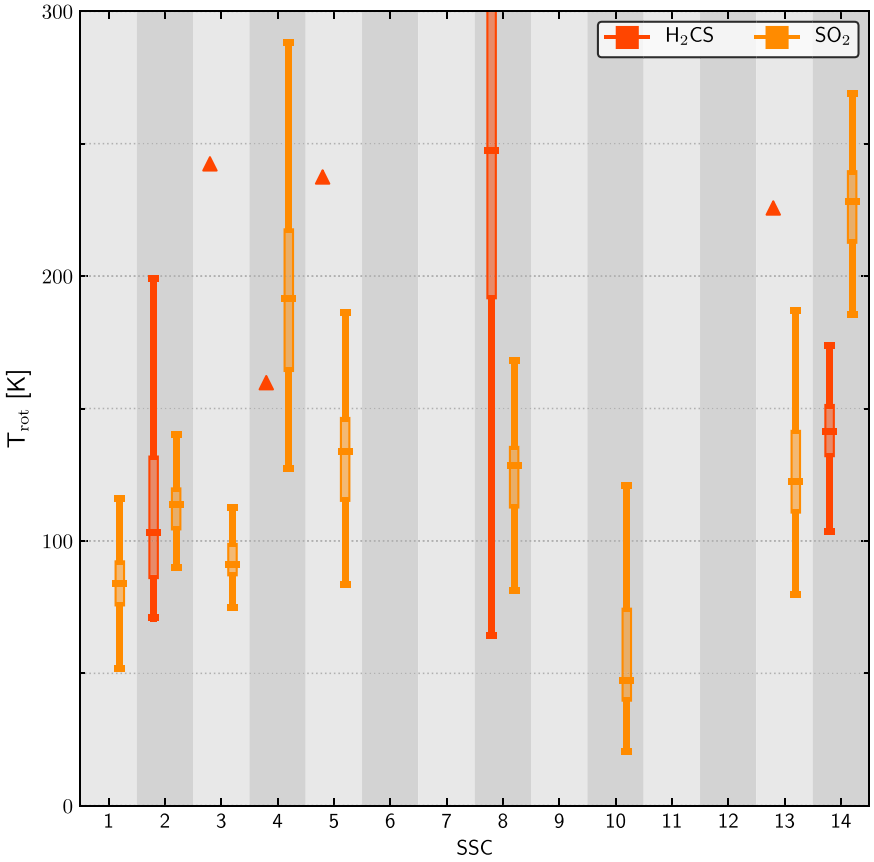

Figure 4. Comparison of the rotational temperatures derived from SO_2 and H_2CS. Boxplots show the distribution of the 100 fit iterations: a vertical line extends over the full range of values, and the second and third quartiles are represented by a box with the median shown as a horizontal line. Triangles represent lower limits (16th percentile) in the cases where the temperature is weakly constrained.

low. The detected H_2CS lines only allow for a robust temperature estimation in SSCs 2, 8, and 14 while in SSCs 3, 4, 5, and 13, T_{rot} it is weakly constrained, and we report lower limits of the obtained XCLASS results.

The rotational temperatures inferred from SO_2 and H_2CS (where possible as discussed above) do only partially agree (SSCs 2, 4, and 8). In SSCs 3, 5, and 13, the lower limits on H_2CS temperature are substantially higher than the inferred SO_2 temperature. In SSC 14, T_{rot} is ∼85 K higher in SO_2 than in H_2CS. It must be stressed here that further radiative transfer modeling is required to translate T_{rot} to kinetic gas temperature T_{kin} and allow for fair comparison across species. Rotational temperatures provide a lower limit to the kinetic gas temperature. For a physical interpretation, it must be considered that SO_2 is fitted with optical depths of 3 to >5 in all SSCs. All reported temperatures thus correspond to outer gas layers of an SSC rather than its core temperature, which might be different due to internal heating (e.g., feedback).

The mean rotational temperature over the SSCs with good estimates is 127 K in SO_2. The common excitation temperature of 130 K assumed for all other rotational species is therefore a good common estimate. The molecular gas in SSC 14 is most likely significantly hotter than in the other SSCs. This is in line with the rich chemistry (high species detection rate) and in most regards more extreme nature of this source. Similarly, SSC 10, the coolest SSC in the sample, is among the faintest SSCs in most lines and has low line detection rates. SSC 4 shows surprisingly high temperatures given that it is average in all other quantities in this study and L18. The other SSCs are similar in temperature at ∼90 K (SSC 1 and 3) or ∼115–130 K (SSC 2, 5, 8, and 13).

In the CMZ of the Milky Way, an environment similar to the center of NGC 253, Tanaka et al. (2018) found a strong positive correlation of HC_3N (10–9) with temperature. If this correlation extends to high-J lines of HC_3N, it would imply a high temperature in SSC 14, somewhat elevated temperatures in SSC 5 and 13, but lower temperatures in SSCs 1, 2, 3, 4, 8, 9, 10, 11, and 12. For SSC 6 and 7, neither of the two HC_3N lines are detected. Such an HC_3N–temperature correlation is not present in our data. SSC 14 is indeed hot and bright in HC_3N, but there are no elevated temperatures in SSC 5 and 13. The high temperature in SSC 4 is matched by HC_3N line brightness and column density marginally different from SSC 2 or 3 with much lower temperatures. Hence, a potential HC_3N—temperature correlation does not extend to the high-J lines ($J_u = 38$ with $T_{ex} = 307$ K and $J_u = 39$ with $T_{ex} = 323$ K) that we observed here.

Our results of an average $T_{rot} \sim 130$ K are consistent with Rico-Villas et al. (2020), the only other temperature measurement on cluster scales, who find HC_3N rotational temperatures of 107 ± 22 K to 125 ± 45 K and dust temperatures of 200–375 K. Considering that T_{rot} is a lower limit to T_{kin}, the molecular gas is at similar temperatures to the dust and probably thermally coupled.

5. Summary

We present high-resolution ALMA observations of the SSCs in the starbursting center of NGC 253. Our spectral setup in band 7 covers a wealth of molecular species and pushes at

resolving the compact (proto-)super star clusters with 2.5 pc spatial resolution. In spectra focused on the SSCs, we detect up to 55 lines of 19 species. Modeling the spectra with XCLASS allows us to independently study observation-based line ratios and modeled physical quantities.

The SSCs differ significantly in chemical complexity between four and 19 detected species. In CO, HCN, HCO^+, and CS, we detect multiple components and potential signs of self-absorption in HCN and HCO^+ in four SSCs. The other species are associated in velocity with the same CO/HCN/HCO^+/CS component or the absorption component of present.

The line ratios CO/HCN and CO/HCO^+ of ∼1–10 are low, implying high dense gas fractions. HCN/HCO^+ is consistent with unity in all but one cluster, which is most likely caused by high opacity. CS/HCN scatters significantly across SSCs and does not correlate with other properties aside from the number of detected species. Its tracer properties remain unclear.

All SSCs favor PDR chemistry over XDR chemistry as indicated by combinations of the line ratios of HCN, HCO^+, HNC, and CS in comparison to models (Loenen et al. 2008; Baan et al. 2008). According to these models, our data favors densities of $\sim 10^5\,\mathrm{cm}^{-3}$. The SSCs close to the central SMBH at projected distances <8.5 pc are inconsistent with XDR chemistry induced by a potential low-luminosity AGN. NGC 253's putative AGN continues to be elusive.

Opacities derived from HCN and $HC^{13}N$ fall in the high optical depth regime with $\tau \gtrsim 1$ to $\tau > 10$ in HCN and up to $\tau = 0.3$ in $H^{13}CN$ and $HC^{15}N$.

We detect bright HC_3N in highly excited states in many SSCs, which implies high IR radiation fields and gas temperatures. This is at odds with finding PDR chemistry, as the UV flux in PDRs can dissociate HC_3N. Potential solutions to this discrepancy are that mechanical heating dominates the energy input over a weak UV field or detected HC_3N and HCN/HCO^+/HNC/CS emission originates from different locations in the cloud governed by opacity.

Vibrationally excited lines of HCN and HC_3N are frequently detected (in six to eight of 14 SSCs) in our observations. The fraction of vibrational excitation of a rotational state can be significant in some SSCs of the order of 10%–30%. The excitation of these lines is likely caused by strong IR radiation fields that are trapped by a greenhouse effect due to high continuum opacities.

The gas in the SSCs is hot as indicated by SO_2 rotational temperatures of ∼130 K on average.

The presented observations demonstrate the power of ALMA to zoom into some of the most actively star-forming regions in the local universe.

The authors would like to thank the anonymous referee for a detailed report that significantly improved this paper.

The work of A.K.L. is partially supported by NASA ADAP grants NNX16AF48G and NNX17AF39G and the National Science Foundation under grant Nos. 1615105, 1615109, and 1653300. The work of EACM is supported by the National Science Foundation under grant No. AST-1813765.

This paper makes use of the following ALMA data: ADS/JAO.ALMA #2015.1.00274.S. ALMA is a partnership of ESO (representing its member states), NSF (USA) and NINS (Japan), together with NRC (Canada), NSC and ASIAA (Taiwan), and KASI (Republic of Korea), in cooperation with the Republic of Chile. The Joint ALMA Observatory is operated by ESO, AUI/NRAO, and NAOJ. The National Radio Astronomy Observatory is a facility of the National Science Foundation operated under cooperative agreement by Associated Universities, Inc.

Software: CASA (McMullin et al. 2007), Astropy (Astropy Collaboration et al. 2013, 2018), XCLASS (Möller et al. 2018).

Appendix A
Details of XCLASS Fitting

A.1. Handling of Blended Lines in the First Fit Run

Joint fitting of multiple species with insufficient constraints increases the number of degrees of freedom to a point where the fitter does not converge reliably anymore. We therefore fit the species listed in Table 1 independently where possible or include potential blended lines in the fit if necessary. For CO, CS, HCN, HCO+, H2CS, $H^{13}CN$, $HC^{15}N$, $H^{15}NC$, SO, ^{33}SO, SO_2, and HCN ($\nu_2 = 1$), completely independent fitting is possible with an appropriately selected fit range. The other species HCN ($\nu_2 = 2'$), HC_3N ($\nu = 0'$), HC_3N ($\nu_6 = 1'$), HC_3N ($\nu_6 = 2'$), HC_3N ($\nu_7 = 1'$), HC_3N ($\nu_7 = 2'$), ^{34}SO ($\nu = 0'$), $S^{18}O$ ($\nu = 0'$), and $^{34}SO2$ ($\nu = 0'$) must be fitted jointly with lines of other species.

A.2. XCLASS Fit Parameters

XCLASS models the spectra based on the molecular parameters of the species to be fitted and can directly solve for physical quantities such as rotational (vibrational) temperature and column density. Further fit parameters are linewidth and centroid of the line. As we work with single-pixel spectra, we leave the additional *source size parameter* fixed at unity. This assumes the source to completely fill the beam ($0\farcs13 \times 0\farcs17$, ∼2.5 pc) as is indicated by the SSC sizes of ∼1.5–4 pc obtained by L18.

XCLASS allows us to fit for *excitation temperature* even when only one line of a species is detected due to the effect on the line shape (e.g., flattening due to opacity). However, with a single transition, the temperature cannot be well constrained, and the results scatter wildly. The fitted excitation temperature in such a case strongly depends on the line shape, which is easily influenced by random noise fluctuations. For the species with only a single line detected, we therefore need to fix the temperature. In the case of multiple detected lines (SO_2, H_2CS), the temperature also scatters considerably and sometimes even provides unphysical results (e.g., higher than the molecular binding energy) when the fit fails to converge successfully. Hence, we fix the rotational temperature $T_{\rm rot} = 130$ K, which is the temperature of the warm ISM component found by Mangum et al. (2013) and Gorski et al. (2017) at lower spatial resolution. Assuming this temperature keeps our analysis consistent with L18 who also assumed 130 K. The observed CO peak brightness temperature $T_{\rm b} = 60$–130 K may act as a proxy for $T_{\rm rot}$ under certain assumptions (optically thick emission, beam filling factor unity). Since we measure $T_{\rm rot} \sim 130$ K (Section 4.5), one of these assumptions is not met. The excitation temperature $T_{\rm vib}$ of vibrationally excited species is certainly higher but difficult to estimate. Line ratios of vibrational states with differing $E_{\rm upper}$ (or $E_{\rm lower}$) could place limits on $T_{\rm vib}$, but in many SSCs, no vibrationally excited species are detected. We therefore use a common fixed excitation temperature of $T_{\rm vib} = 300$ K. This value is supposedly on the lower side of the actual excitation temperatures and thus causes the column densities of the vibrationally excited states to be on the higher

side. The observed emission intensity is influenced by temperature and column density because higher excitation and more emitting molecules provide stronger line emission. In SO_2, the most reliable temperature tracer in our sample, changes in temperature and column density are inversely correlated at ratios of 0.8–1.0 in the SSCs with successful temperature estimation (see Section 4.5). This means any under-/overestimation of the fixed temperatures by a factor x directly translates to an x times under-/overestimation in column density. A factor of two variation in the chosen excitation temperature ($65\,\mathrm{K} < T_{\mathrm{rot}} < 260\,\mathrm{K}$ and $150\,\mathrm{K} < T_{\mathrm{vib}} < 600\,\mathrm{K}$) is very plausible in the SSCs. Hence, the derived column densities should be understood with a systematic error of a factor of two.

We apply loose limits on column density (10^{12}–$10^{25}\,\mathrm{cm}^{-2}$), linewidth (5–80 $\mathrm{km\,s}^{-1}$), and line centroid (-10–$10\,\mathrm{km\,s}^{-1}$ relative to the first manual estimate in Section 2.2). For the second run, these are limited to the 16th–84th percentile ranges of the first run.

A.3. Fit Algorithm

XCLASS offers a choice of algorithms that can be daisy-chained to allow for faster and more robust exploration of the parameter space depending on the data set. For this data set, the fitting generally works well and is robust against repetition of the fit and variations of the initial guesses. For some species in a few SSCs, it is necessary to adjust initial guesses or boundaries of the fit parameters to allow the algorithm to find a solution. We use a combination of two algorithms in sequence to assure the solver finds the global minimum of the fit and then converges to this minimum. We achieve this by a combination of 50 iterations of the "Genetic" algorithm followed by 50 iterations of the "Levenberg-Marquardt" algorithm. For a detailed description of the fit algorithms, we refer to Möller et al. (2018).

A.4. Error Estimation

This XCLASS fitting procedure reliably finds the best fit but does not estimate errors of the fit parameters. We therefore bootstrap the errors using a Monte Carlo scheme: we draw 100 versions of Gaussian noise and add it to the observed spectra, which are then fitted as described above. The added Gaussian noise is set up with standard deviation 0.46 K, the measured rms noise in the data. This scheme tests the robustness of the fit to noise fluctuations in the data and thus the statistical error of the fit. Systematic errors such as the flux uncertainty of $\lesssim$5% for ALMA observations (ALMA Technical Handbook) apply additionally. Of the 100 fit variations plus a fit to the unaltered spectra, we report the median and 16th–84th percentiles range[15] as a best estimate and respective error margin for each parameter.

Appendix B
SSC Energy Source Using Line Intensity Ratios

As discussed in Section 4.2.5, the model by Loenen et al. (2008) and Baan et al. (2008) provides a tool to estimate the excitation environment in the SSCs, which can then be interpreted for the potential energy sources. Since we derive column densities with XCLASS, we can directly use physical quantities for this analysis instead of observational quantities. As a test, however, we also construct the ratio diagrams for line ratios in Figure B1. Note that, in this case, the correction of the observed $H^{15}NC$ to $H^{14}NC$ is only an approximation because we do not consider optical depth but only the observed line intensity ratios. Nonetheless, we arrive at the same conclusion that the chemistry in the SSCs is powered by PDRs rather than XDRs. The exact placement in the ratio–ratio planes is slightly different, though, with deviations of ~0.1–0.2 dex. SSCs 2 and 3 are not compatible with XDR conditions, which was barely the case for the column density ratios (Figure 3).

The density estimation deviates between the estimation from line ratios and column density ratios. The CS/HCN line ratios are consistently <1, suggesting $N_H < 10^{22}\,\mathrm{cm}^{-2}$. This is in tension with the fact that the SSCs are undetected at IR wavelengths and thus must be hidden behind large columns of gas and dust. The assumption made by Baan et al. (2008) that integrated line ratios have the same diagnostic value as column density ratios is thus not valid, at least in the case of NGC 253's SSCs.

As in Section 4.2.5, we overplot the measurement from Baan et al. (2008; central 440 pc) and the 10 selected regions from Meier et al. (2015; 40 pc). As opposed to the column density ratios (Figure 3), the large-scale measurement of Baan et al. (2008) deviates from the SSCs toward higher HNC/HCO^+ and slightly lower HCO^+/HCN but is still close to the ratios in SSCs 2 and 3. Arguably, this is caused by the large amount of molecular gas outside the SSCs that we focus on. The regions by Meier et al. (2015) are consistent with our measurements in HNC/HCN versus HNC/HCO^+ but are offset toward lower HCO^+/HCN by ~0.1 as seen in the upper two panels. This is most likely a systematic effect in the measured HCN or HCO^+ intensities.

[15] The 16th–84th percentiles range corresponds to -1σ to $+1\sigma$ for Gaussian distributions.

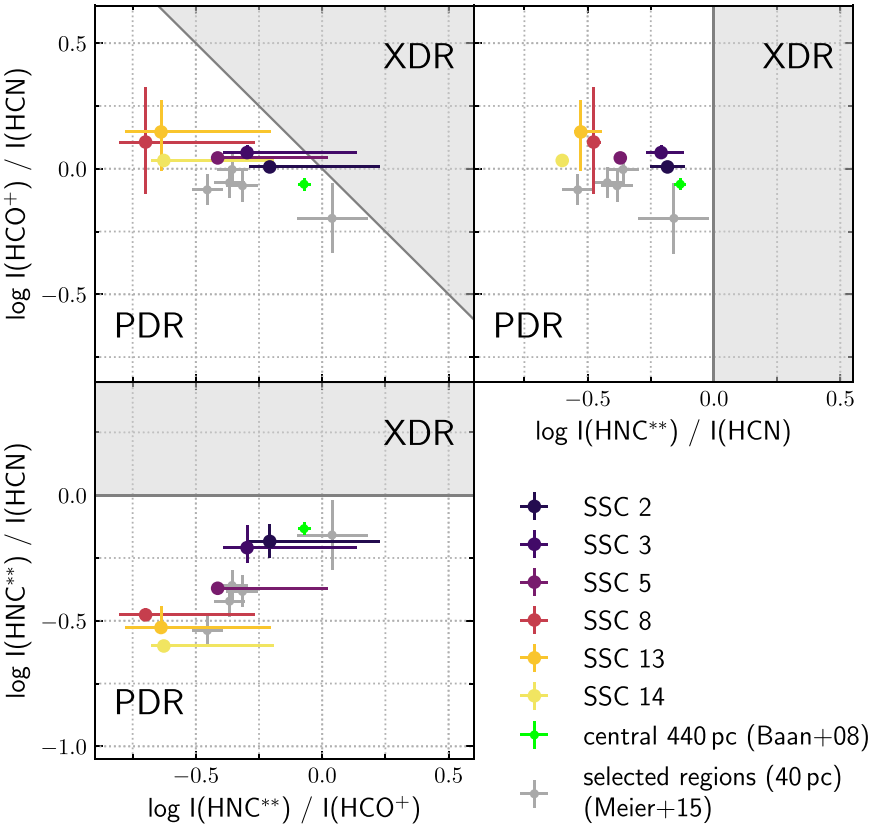

Figure B1. PDR–XDR chart according to Loenen et al. (2008) and Baan et al. (2008) for ratios of HCN, HCO^+, and HNC intensities. In our observations, we do not observe $H^{14}NC$ but $H^{15}NC$, which we estimate using the isotope ratio $^{14}N/^{15}N$ from $H^{14}NC$ and $H^{15}NC$. In the plots, this is marked by the ** symbol. The correction is possible for only six out of 14 SSCs due to the detection rate of $H^{15}NC$. The Baan et al. (2008) estimate for the central region of NGC 253 extends over all SSCs and surrounding gas.

ORCID iDs

Nico Krieger https://orcid.org/0000-0003-1104-2014
Alberto D. Bolatto https://orcid.org/0000-0002-5480-5686
Adam K. Leroy https://orcid.org/0000-0002-2545-1700
Rebecca C. Levy https://orcid.org/0000-0003-2508-2586
Elisabeth A. C. Mills https://orcid.org/0000-0001-8782-1992
David S. Meier https://orcid.org/0000-0001-9436-9471
Jürgen Ott https://orcid.org/0000-0001-8224-1956
Sylvain Veilleux https://orcid.org/0000-0002-3158-6820
Fabian Walter https://orcid.org/0000-0003-4793-7880
Axel Weiß https://orcid.org/0000-0003-4678-3939

References

Aalto, S., Garcia-Burillo, S., Muller, S., et al. 2012, A&A, 537, A44
Aalto, S., Martin, S., Costagliola, F., et al. 2015, A&A, 584, A42
Aalto, S., Monje, R., & Martin, S. 2007a, A&A, 475, 479
Aalto, S., Polatidis, A. G., Hüttemeister, S., & Curran, S. J. 2002, A&A, 381, 783
Aalto, S., Spaans, M., Wiedner, M. C., & Hüttemeister, S. 2007b, A&A, 464, 193
Aladro, R., Martin-Pintado, J., Martin, S., Mauersberger, R., & Bayet, E. 2011, A&A, 525, A89
Aladro, R., Martin, S., Riquelme, D., et al. 2015, A&A, 579, A101
Ando, R., Nakanishi, K., Kohno, K., et al. 2017, ApJ, 849, 81
Astropy Collaboration, Price-Whelan, A. M., Sipőcz, B. M., et al. 2018, AJ, 156, 123
Astropy Collaboration, Robitaille, T. P., Tollerud, E. J., et al. 2013, A&A, 558, A33
Baan, W. A., Henkel, C., Loenen, A. F., Baudry, A., & Wiklind, T. 2008, A&A, 477, 747
Bendo, G. J., Beswick, R. J., D'Cruze, M. J., et al. 2015, MNRAS, 450, L80
Bolatto, A. D., Warren, S. R., Leroy, A. K., et al. 2013, Natur, 499, 450
Charnley, S. B. 1997, ApJ, 481, 396
Costagliola, F., & Aalto, S. 2010, A&A, 515, A71
Costagliola, F., Aalto, S., Rodriguez, M. I., et al. 2011, A&A, 528, A30
Davis, B. L., Berrier, J. C., Johns, L., et al. 2014, ApJ, 789, 124
de Vicente, P., Martin-Pintado, J., Neri, R., & Colom, P. 2000, A&A, 361, 1058
Falstad, N., Aalto, S., Mangum, J. G., et al. 2018, A&A, 609, A75
Gallagher, M. J., Leroy, A. K., Bigiel, F., et al. 2018, ApJ, 858, 90
Gao, Y., & Solomon, P. M. 2004, ApJS, 152, 63
Goldsmith, P. F., Krotkov, R., Snell, R. L., Brown, R. D., & Godfrey, P. 1983, ApJ, 274, 184
González-Alfonso, E., & Sakamoto, K. 2019, ApJ, 882, 153
Gorjian, V., Turner, J. L., & Beck, S. C. 2001, ApJ, 554, L29
Gorski, M., Ott, J., Rand, R., et al. 2017, ApJ, 842, 124
Graedel, T. E., Langer, W. D., & Frerking, M. A. 1982, ApJS, 48, 321
Graninger, D. M., Herbst, E., Öberg, K. I., & Vasyunin, A. I. 2014, ApJ, 787, 74
Günthardt, G. I., Agüero, M. P., Camperi, J. A., et al. 2015, AJ, 150, 139
Hatchell, J., Thompson, M. A., Millar, T. J., & MacDonald, G. H. 1998, A&A, 338, 713
Heckman, T. M., Lehnert, M. D., Strickland, D. K., & Armus, L. 2000, ApJS, 129, 493
Henkel, C., Asiri, H., Ao, Y., et al. 2014, A&A, 565, A3
Holtzman, J. A., Faber, S. M., Shaya, E. J., et al. 1992, AJ, 103, 691
Huettemeister, S., Henkel, C., Mauersberger, R., et al. 1995, A&A, 295, 571
Imanishi, M., Nakanishi, K., & Izumi, T. 2016, ApJ, 825, 44
Imanishi, M., Nakanishi, K., & Izumi, T. 2017, ApJ, 849, 29
Imanishi, M., Nakanishi, K., Tamura, Y., & Peng, C.-H. 2009, AJ, 137, 3581
Izumi, T., Kohno, K., Aalto, S., et al. 2016, ApJ, 818, 42
Izumi, T., Kohno, K., Martín, S., et al. 2013, PASJ, 65, 100
Jackson, J. M., Paglione, T. A. D., Carlstrom, J. E., & Rieu, N.-Q. 1995, ApJ, 438, 695
Jiménez-Donaire, M. J., Bigiel, F., Leroy, A. K., et al. 2017, MNRAS, 466, 49
Kauffmann, J., Goldsmith, P. F., Melnick, G., et al. 2017, A&A, 605, L5

Knudsen, K. K., Walter, F., Weiß, A., et al. 2007, ApJ, 666, 156
Kohno, K., Matsushita, S., Vila-Vilaró, B., et al. 2001, in ASP Conf. Proc. 249, The Central Kiloparsec of Starbursts and AGN: The La Palma Connection, ed. J. H. Knapen et al. (San Francisco, CA: ASP), 672
Kornei, K. A., & McCrady, N. 2009, ApJ, 697, 1180
Krieger, N., Bolatto, A. D., Walter, F., et al. 2019, ApJ, 881, 43
Krips, M., Neri, R., Garcia-Burillo, S., et al. 2008, ApJ, 677, 262
Leroy, A. K., Bolatto, A. D., Ostriker, E. C., et al. 2015, ApJ, 801, 25
Leroy, A. K., Bolatto, A. D., Ostriker, E. C., et al. 2018, ApJ, 869, 126
Lindberg, J. E., Aalto, S., Costagliola, F., et al. 2011, A&A, 527, A150
Liu, H. B., Jimenez-Serra, I., Ho, P. T. P., et al. 2012, ApJ, 756, 10
Loenen, A. F., Spaans, M., Baan, W. A., & Meijerink, R. 2008, A&A, 488, L5
Mangum, J. G., Darling, J., Henkel, C., et al. 2013, ApJ, 779, 33
Mangum, J. G., Ginsburg, A. G., Henkel, C., et al. 2019, ApJ, 871, 170
Martin, S., Aladro, R., Martin-Pintado, J., & Mauersberger, R. 2010, A&A, 522, A62
Martin, S., Kohno, K., Izumi, T., et al. 2015, A&A, 573, A116
Martin, S., Krips, M., Martin-Pintado, J., et al. 2011, A&A, 527, A36
Martin, S., Martin-Pintado, J., Mauersberger, R., Henkel, C., & Garcia-Burillo, S. 2005, ApJ, 620, 210
Martín, S., Martin-Pintado, J., & Viti, S. 2009, ApJ, 706, 1323
Martin, S., Mauersberger, R., Martin-Pintado, J., Henkel, C., & Garcia-Burillo, S. 2006, ApJS, 164, 450
Martin, S., Muller, S., Henkel, C., et al. 2019, A&A, 624, A125
McCrady, N., Graham, J. R., & Vacca, W. D. 2005, ApJ, 621, 278
McMullin, J. P., Waters, B., Schiebel, D., Young, W., & Golap, K. 2007, in ASP Conf. Proc. 376, adass XVI, ed. R. Shaw, F. Hill, & D. J. Bell (San Francisco, CA: ASP), 127
Meier, D. S., & Turner, J. L. 2005, ApJ, 618, 259
Meier, D. S., Turner, J. L., & Schinnerer, E. 2011, AJ, 142, 32
Meier, D. S., Walter, F., Bolatto, A. D., et al. 2015, ApJ, 801, 63
Meijerink, R., & Spaans, M. 2005, A&A, 436, 397
Meijerink, R., Spaans, M., & Israel, F. P. 2006, ApJ, 650, L103
Meijerink, R., Spaans, M., & Israel, F. P. 2007, A&A, 461, 793
Mills, E. A. C., & Battersby, C. 2017, ApJ, 835, 76
Minh, Y. C., Liu, H. B., & Galván-Madrid, R. 2016, ApJ, 824, 99
Möller, T., Endres, C., & Schilke, P. 2018, XCLASS: eXtended CASA Line Analysis Software Suite v1.2.5, Astrophysics Source Code Library, ascl:1810.016
Müller, H. S. P., Schlöder, F., Stutzki, J., & Winnewisser, G. 2005, JMoSt, 742, 215
Müller-Sánchez, F., González-Martin, O., Fernández-Ontiveros, J. A., Acosta-Pulido, J. A., & Prieto, M. A. 2010, ApJ, 716, 1166
Ott, J., Weiß, A., Henkel, C., & Walter, F. 2005, ApJ, 629, 767
Paglione, T. A. D., Jackson, J. M., & Ishizuki, S. 1997, ApJ, 484, 656
Paglione, T. A. D., Wall, W. F., Young, J. S., et al. 2001, ApJS, 135, 183
Paglione, T. A. D., Yam, O., Tosaki, T., & Jackson, J. M. 2004, ApJ, 611, 835
Pety, J., Guzmán, V. V., Orkisz, J. H., et al. 2017, A&A, 599, A98
Pickett, H. M., Poynter, R. L., Cohen, E. A., et al. 1998, JQSRT, 60, 883
Portegies Zwart, S. F., McMillan, S. L. W., & Gieles, M. 2010, ARA&A, 48, 431
Privon, G. C., Herrero-Illana, R., Evans, A. S., et al. 2015, ApJ, 814, 39
Rekola, R., Richer, M. G., McCall, M. L., et al. 2005, MNRAS, 361, 330
Remijan, A. J., Markwick-Kemper, A., & Frequencies, A. W. G. o. S. L. 2007, AAS, 211, 132.11
Rico-Villas, F., Martin-Pintado, J., González-Alfonso, E., Martin, S., & Rivilla, V. M. 2020, MNRAS, 491, 4573
Rodríguez-Rico, C. A., Goss, W. M., Zhao, J. H., Gómez, Y., & Anantharamaiah, K. R. 2006, ApJ, 644, 914
Rolffs, R., Schilke, P., Wyrowski, F., et al. 2011a, A&A, 529, A76
Rolffs, R., Schilke, P., Wyrowski, F., et al. 2011b, A&A, 527, A68
Rolffs, R., Schilke, P., Zhang, Q., & Zapata, L. 2011c, A&A, 536, A33
Sakamoto, K., Aalto, S., Costagliola, F., et al. 2013, ApJ, 764, 42
Sakamoto, K., Aalto, S., Evans, A. S., Wiedner, M. C., & Wilner, D. J. 2010, ApJL, 725, L228
Sakamoto, K., Mao, R.-Q., Matsushita, S., et al. 2011, ApJ, 735, 19
Schilke, P., Walmsley, C. M., Pineau des Forêts, G., et al. 1992, A&A, 256, 595
Sharp, R. G., & Bland-Hawthorn, J. 2010, ApJ, 711, 818
Shirley, Y. L. 2015, PASP, 127, 299
Sorai, K., Nakai, N., Kuno, N., Nishiyama, K., & Hasegawa, T. 2000, PASJ, 52, 785
Strickland, D. K., Heckman, T. M., Weaver, K. A., & Dahlem, M. 2000, AAS, 5, 15.14
Strickland, D. K., Heckman, T. M., Weaver, K. A., Hoopes, C. G., & Dahlem, M. 2002, ApJ, 568, 689
Sturm, E., González-Alfonso, E., Veilleux, S., et al. 2011, ApJL, 733, L16
Tanaka, K., Nagai, M., Kamegai, K., Iino, T., & Sakai, T. 2018, ApJS, 236, 40
Tang, X. D., Henkel, C., Menten, K. M., et al. 2019, A&A, 629, A6
Turner, B. E. 1985, ApJ, 299, 312
Ulvestad, J. S., & Antonucci, R. R. J. 1997, ApJ, 488, 621
van der Tak, F. F. S., Black, J. H., Schöier, F. L., Jansen, D. J., & van Dishoeck, E. F. 2007, A&A, 468, 627
Viti, S., Fontani, F., Jimenez-Serra, I., & Holdship, J. 2019, MNRAS, 486, 4805
Walter, F., Bolatto, A. D., Leroy, A. K., et al. 2017, ApJ, 835, 265
Watson, A. M., Gallagher, J. S. I., Holtzman, J. A., et al. 1996, AJ, 112, 534
Westmoquette, M. S., Smith, L. J., & Gallagher, J. S., III 2011, MNRAS, 414, 3719
Whitmore, B. C. 2003, in Proc. Space Telescope Science Institute Symp., A Decade of Hubble Space Telescope Science, ed. M. Livio et al. (Cambridge: Cambridge Univ. Press), 153
Wright, M. C. H., Plambeck, R. L., & Wilner, D. J. 1996, ApJ, 469, 216
Wyrowski, F., Güsten, R., Menten, K. M., et al. 2016, A&A, 585, A149
Wyrowski, F., Schilke, P., & Walmsley, C. M. 1999, A&A, 341, 882
Ziurys, L. M., & Turner, B. E. 1986, ApJ, 300, L19